Middle to late Miocene growth of the North Pamir

Lin Li[1,2,3*], Guillaume Dupont-Nivet[1,4], Yani Najman[5], Mustafa Kaya[4], Niels Meijer[4], Marc Poujol[1], Jovid Aminov[6,7]

[1]University of Rennes, CNRS, Géosciences Rennes-UMR 6118, Rennes, France

[2]College of Science, Rochester Institute of Technology, Rochester, NY, USA

[3]Department of Geosciences, University of Arizona, Tucson, USA

[4]Institute of Geosciences, Potsdam University, Potsdam, Germany

[5]Lancaster Environment Centre, Lancaster University, Lancaster, UK

[6]Institute of geology, earthquake engineering and seismology, Academy of Sciences, Dushanbe, Republic of Tajikistan

[7]Institute of Tibetan Plateau Research and Center for Excellence in Tibetan Plateau Earth Sciences, Chinese Academy of Sciences, Beijing, China

[*]Corresponding author email: li.lin8611@gmail.com.

Highlights:

- A regional lithofacies shift in the eastern Tajik Basin is magnetostratigraphically-dated to the middle Miocene
- Provenance and stable isotopic data suggest middle–late Miocene deformation and surface uplift of the North Pamir
- Middle–late Miocene growth of the North Pamir has implications for Asian tectonic and climate evolution

Keywords: Tajik Basin; Pamir; Lithostratigraphy; Magnetostratigraphy; Provenance; Stable isotopes

Abstract

How and when the Pamir formed remains an open question. This study explores Pamir tectonics recorded in a sedimentary section in the eastern Tajik Basin. A prominent lithofacies change that has been recognized regionally is assigned to the middle Miocene (13.5 Ma based on preferred magnetostratigraphic correlation). Closely following this change, detrital zircon U-Pb age spectra and mudstone bulk-rock ε_{Nd} values exhibit a sediment source change from the Central to the North Pamir estimated ca. 12 Ma. At the same time, the stable oxygen and carbon isotopic values of carbonate cements show negative and positive shifts, respectively. Combined with previous studies in both the Tajik and Tarim basins, these results suggest that the North Pamir experienced a middle–late Miocene phase of deformation and surface uplift. This supports models proposing middle–late Miocene Pamir tectonism, and climate models implying that coeval Pamir orogenesis deflected Westerly moisture and affected Asian environments.

1. Introduction

The Pamir mountains at the western end of the Himalayan-Tibetan orogen have experienced the tectonic effects of the indentation of India into Asia during the Cenozoic (Burtman & Molnar, 1993; Yin & Harrison, 2000). Compared to the east-west trending northern margin of the Tibetan Plateau to the east and the Hindu Kush Mountains to the west, the Pamir stands at similarly high elevations but exhibits a prominent northward arcuate shape known as the Pamir salient, involving curved tectonic elements of terranes, sutures, and faults (Fig. 1A; Robinson et al., 2004; Schwab et al., 2004).

Different models have been proposed to explain the formation of the Pamir salient. One group of models suggest that the salient shape was formed as a result of large scale (>300 km) northward overthrusting, in association with the southward continental subduction of the Tajik-Tarim mantle lithosphere and lower crust since the Paleogene India-Asia collision (Burtman & Molnar, 1993) or since 25–20 Ma (Sobel et al., 2013). The other group of models proposes that the salient shape is largely inherited from pre-Cenozoic tectonics, with no more than 100 km of northward translation during the Cenozoic relative to adjacent Tibet (Chapman et al., 2017; Chen et al., 2018; Li et al., 2020; Rembe et al., 2021). Based on the differences in subsurface process and initiation timing, this group of models can be further divided into two sub-groups: either resumed northward indentation of the Indian mantle lithosphere forced delamination of the Asian mantle lithosphere and lower crust (including both Tajik-Tarim and North Pamir) and deformed to some extent the Pamir upper crust into its salient shape since 12–10 Ma (Kufner et al., 2016; Rutte et al., 2017; Abdulhameed et al., 2020); or delamination of the mantle lithosphere and lower crust of the Pamir terranes (South, Central, and North Pamir) with a more limited northward translation of the North Pamir and crustal deformation in the Tajik Basin since 25–20 Ma (Chapman et al., 2017).

Sedimentary deposits around active orogenic belts archive abundant information about the timing and propagation of deformation as well as source terrane tectonics that can help distinguish between the above-mentioned different models. To that end, clarifying the ages of deposition as well as timings of lithofacies and provenance shifts in surrounding basins of the Pamir salient (Fig. 1A) has been performed in both the Tarim (e.g., Bershaw et al., 2012; Sun & Jiang, 2013; Zheng et al., 2015; Blayney et al., 2016; Sun et al., 2016; Blayney et al., 2019) and Tajik basins (e.g., Klocke et al., 2017; Chapman et al., 2019; Dedow et al., 2020; Sun et al., 2020; Wang et al., 2020). In the north-central Tajik Basin, a ca. 25 Ma wetting signal has been associated with the coeval drying signal in the Tarim basin, which together was interpreted to reflect Pamir surface uplift and northward indentation that intercepted the dominant Westerly moisture flow (Wang et al., 2019; Wang et al., 2020). Nevertheless, the widely spread Neogene sedimentary successions in the eastern Tajik Basin remains poorly studied and virtually unconstrained in age, despite recording a prominent regional lithofacies change that has been attributed to foreland-ward propagation of deformation in the Pamir (Klocke et al., 2017; Chapman et al., 2019; Dedow et al., 2020).

This study reports a new magnetostratigraphically-dated sedimentary section in the eastern Tajik Basin, used to constrain the age of the lithofacies change and further explore its significance with the following datasets. We combined sedimentological observations documenting depositional environment changes, with detrital zircon U-Pb ages and mudstone bulk-rock ε_{Nd} values recording provenance shifts, and carbonate cement stable oxygen and carbon isotopic values to infer topographic and environmental evolution.

2. Geologic background

2.1. The Pamir

The Pamir today forms a northward salient bounded by the Tarim Basin to the east and the Tajik Basin to the west. To the north, it is separated from the southwest Tian Shan by the Alai Basin (Fig. 1A). The Pamir is divided into the North, Central, and South Pamir terranes (e.g., Schwab et al., 2004; Villarreal et al., 2020). Because of their different geological histories, these terranes provide distinctive sources for the detritus deposited in the Tajik Basin.

The South and Central Pamir are both Gondwanaland-affiliated terranes, that were accreted to the southern margin of the Asian continent during the Late Triassic Cimmerian Orogeny (e.g., Angiolini et al., 2013; Villarreal et al., 2020). During the latest Triassic–Late Jurassic, the Central and South Pamir served as the passive margin of Asia (Angiolini et al., 2013; Villarreal et al., 2020). During the Early Cretaceous (e.g., 130–90 Ma), the northward subduction of the Neo-Tethys oceanic lithosphere caused extensive arc magmatism in the South Pamir (Aminov et al., 2017; Chapman et al., 2018), and widespread retro-arc shortening in both the South and Central Pamir (Chapman et al., 2018; Kaya et al., 2020). Around ~40 Ma, the Vanj magmatic complex intruded in the Central Pamir (Chapman et al., 2018). Between ~35 and 20 Ma, the Central Pamir experienced major shortening leading to significant crustal thickening, after which gneiss domes started to exhume since the early Miocene (e.g., ~20 Ma), and ended during the latest middle Miocene (~12 Ma; Rutte et al., 2017). In the South Pamir, the Alichur and Shakhdara gneiss domes (Fig. 1A) started to be active at similar timing but lasted until the Pliocene (~4 Ma; Stübner et al., 2013; Worthington et al., 2020).

The North Pamir is an Asian-affiliated terrane and served as the southern active margin of Asia during the late Paleozoic–Late Triassic (Burtman & Molnar, 1993; Rembe et al., 2021). The North Pamir probably experienced crustal shortening and thickening during the mid-Cretaceous, e.g., 130–100 Ma (Robinson et al., 2004). Low-temperature thermochronological data in the northeastern Pamir indicate slow exhumation throughout much of the late Mesozoic (<100 Ma) and Cenozoic, with two punctuated accelerated exhumation phases at 50–40 Ma and 25–16 Ma, respectively (Amidon & Hynek, 2010; Sobel et al., 2013). Another study in the western North Pamir reported apatite fission-track ages between 10.3 and 6.2 Ma (Abdulhameed et al., 2020).

2.2. Stratigraphy of the Tajik Basin

The Tajik Basin has been a foreland basin since the Early Cretaceous (Chapman et al., 2019; Kaya et al., 2020). After the final westward retreat of the proto-Paratethys Sea from the Tajik Basin at ~37 Ma (Kaya et al., 2019; Wang et al., 2019), the Tajik Basin received exclusively terrestrial fluvial-dominated deposits (Klocke et al., 2017; Chapman et al., 2019; Dedow et al., 2020). The post-sea retreat strata in the Tajik Basin are generally divided into the Baldshuan, Chingou, Tavildara, Karanak, and Polizak formations, which have been broadly assigned to the Oligocene–early Miocene, early–middle Miocene, late Miocene, Pliocene, and Pleistocene, respectively, based on sparse fossil assemblages and low-temperature thermochronological ages (e.g., Klocke et al., 2017; Chapman et al., 2019; Dedow et al., 2020). The Baldshuan Formation is further divided into the Shurisay, Kamolin, and Childara members, from oldest to youngest. These lithostratigraphic names were first introduced in the north-eastern Tajik Basin and later applied over the entire basin (original literature in Russian, see a summary in Klocke et al., 2017). Due to the loose usage of these formation names, stratigraphic units with the same name in different parts of the basin do not necessarily represent the same lithofacies or depositional age.

3. Methods

3.1. Lithofacies analysis

We measured and logged a sedimentary section in the eastern Tajik Basin that includes two separate parts (Fig. 1B–C). The Khirmanjo (KH) section spans the Baldshuan Formation and lower Chingou Formation. The Shurobod (SB) section is located ~10 km to the south of the Khirmanjo section and spans only the Chingou Formation.

3.2. Paleomagnetic analysis

Throughout the Khirmanjo (~1800 m thick) and Shurobod (~1400 m thick) sections, a total of 533 oriented paleomagnetic samples were collected at regular intervals targeting the finest lithologies using a battery-powered drill. The analysis was performed in the magnetically shielded room at the Palaeomagnetic Laboratory at the University of Rennes 1. Detailed methodology can be found in Supplementary Text S1. See Supplementary Table S1 for paleomagnetic data.

3.3. Detrital zircon U-Pb analysis

Seven sandstone samples were analyzed for detrital zircon U-Pb geochronology (Fig. 1). Mounted and polished zircons were analyzed by a Teledyne Cetac 193 nm G2 laser ablation (LA) system coupled with an Agilent 7900 inductively coupled plasma mass spectrometer (ICP-MS) quadrupole at the University of Rochester. Half of one sample was analyzed at the University of Rennes 1 using an ESI NWR193UC excimer laser coupled with an Agilent 7700x ICP-MS quadrupole. Detailed methodology can be found in Supplementary Text S2. See Supplementary Table S2 for U-Pb age data.

3.4. Mudstone bulk-rock Sm-Nd isotopic analysis

Twenty-eight mudstone samples were analyzed for bulk-rock neodymium (Nd) isotopic values. Analyses were carried out at the GeOHeLiS Analytical Platform (Géosciences Rennes, OSUR, University of Rennes 1) using a seven collectors Finnigan MAT-262 mass spectrometer. Detailed methodology can be found in Supplementary Text S3. See Supplementary Table S3 for Nd isotopic data.

3.5. Stable oxygen and carbon isotopic analysis

97 mudstone and sandstone samples containing carbonate cement (hereafter referred to as carbonate cement samples) and 3 paleosol nodular carbonate samples were analyzed for stable oxygen and carbon isotopes. Analyses were carried out using a Thermo MAT 253 (at the joint Goethe University–BiK-F Stable Isotope Facility Frankfurt) or Thermo Delta plus XP (at the University of Rochester SIREAL laboratory) attached to a Thermo GasBench II peripheral device. Detailed methodology can be found in Supplementary Text S4. See Supplementary Table S4 for stable isotopic data.

4. Results and interpretations

4.1. Lithostratigraphy

Detailed lithostratigraphy in the eastern and northeastern Tajik Basin has been recently described in the Tavildara (Klocke et al., 2017), Dashtijum (Chapman et al., 2019), and Obi Khudkham sections (Dedow et al., 2020) (See Fig. 1 for locations). In the following, we summarize the major depositional features of the measured Baldshuan and Chingou formations in the Khirmanjo and Shurobod sections. Table 1 lists lithofacies codes and interpretations, and Fig. 2 exhibits detailed stratigraphic columns.

4.1.1. Baldshuan Formation

At the base of the Baldshuan Formation, the Shurisay Member is distinguished from the underlying greenish marine mudstone and limestone by its orange-red color. The member is ~210 thick (Fig. 2A), dominated by thinly bedded (<5 cm) tabular mudstones, locally interbedded with thin (<10 cm) massive to horizontally stratified sandstones (Fig. 3A). Occasionally, grey-colored conglomerate interlayers with horizontal stratification pinch out laterally in a few tens of meters.

The majority of clasts in the conglomerates, dominated by quartzite and granite, are smaller than 0.5 cm, with a few large ones reaching 5–10 cm.

Above the Shurisay Member, the ~130 m thick Kamolin Member is distinguished by its dominance of thick grey-colored conglomerates (Fig. 2A). The conglomerate beds are similar to those in the Shurisay Member in composition, texture, and sedimentary structures, with clear horizontal stratification and tabular-shaped clasts parallel to bedding. The conglomerate beds in this member generally stack together to form thick units and are also more extensive laterally, reaching hundreds of meters. Normal grading was observed occasionally.

The Childara Member is again characterized by fine-grained mudstones, with interbedded sandstones and conglomerates (Fig. 2A). The lower and upper boundaries of the member are placed at ~340 m and ~990 m, respectively, which signify the appearance and disappearance of thick multistory mudstone layers. The lower and middle parts of the member are characterized by tabular mudstones (Fig. 3B), which are generally mottled, with carbonate nodules present in several intervals. Interbedded with the mudstones are coarse-grained sandstones, which exhibit horizontal stratification, planar and trough cross-bedding. Lenticular-shaped conglomerate layers are rare in the lower part but increase toward the top of the member (Fig. 3C). The conglomerates are generally granular and clast-supported with mostly pebble-sized clasts, sub-angular to sub-rounded, and relatively well sorted. Clasts are mainly granites and sandstones, but carbonates and quartzites also exist. The conglomerates show horizontal stratification, and also occasionally show normal grading to sand-sized particles on top, where current ripples were observed. Both erosive and non-erosive bottoms exist in the conglomerate beds.

Interpretation: We interpret the Baldshuan Formation to be deposited mainly in a braided river environment, agreeing with the interpretation of Chapman et al. (2019) in the Dashtijum section. The dominant tabular and thinly-bedded mudstones and sandstones in the Shurisay Member and the lower–middle Childara Member are floodplain-dominated deposits. The lenticular-shaped conglomerates and sandstones, which exhibit trough cross-bedding, were deposited in fluvial channels. The frequently observed horizontal stratification in the conglomerates further suggests deposition as longitudinal bars.

4.1.2. Chingou Formation

Strata of the upper Khirmanjo section (980–1800 m; Fig. 2A) and the entire measured Shurobod section (Fig. 2B) belong to the Chingou Formation. In Khirmanjo, the formation is characterized by very thick clast-supported conglomerates, which are well cemented and show horizontal stratification. Stacked layers can reach more than 50 m thick. Clasts are generally pebble to cobble in size and dominated by red and green sandstones with recycled conglomerate and granite clasts also common. Generally, the clasts are rounded and moderately well sorted, and the long axes of tabular clasts are parallel to bedding. Imbrications with the long-axes transverse to the flow direction are observed. Muddy matrix-supported conglomerates crop out locally, in which clasts are mainly angular to sub-angular. Mudstones generally outcrop as lenticular-shaped strips. At several stratigraphic heights, mudstones are up to a few meters thick, showing ped structures and containing paleosol nodules (Fig. 3D).

The Chingou Formation in the Shurobod section is dominated by interbedded conglomerate and mudstone layers (Fig. 3F). The conglomerates are mainly clast-supported, tabular shaped, with both erosive (Fig. 3H) and non-erosive bases; the clasts are dominated by red and green sandstones, with minor granite clasts. Less common are matrix-supported conglomerates with angular to sub-angular clasts (Fig. 3G), in which both normal and inverse grading were observed. A distinct part of the section (130–480 m) is dominated by stacked conglomerate layers that reach hundreds of meters thick, which are very poorly sorted with angular, boulder-sized clasts as large as 1–2 m (Fig. 3E), in which mudstones only outcrop as thin lenses (<30 cm).

Interpretation: Two different depositional environments can be identified in the Chingou Formation. Between 130 and 480 m of the Shurobod section, the succession shows features of matrix-support, poor sorting, and angular to sub-angular clasts as large as 2 m, which we interpret as debris-flow deposits in an alluvial fan environment. In contrast, the majority of the formation is dominated by clast-supported and horizontally stratified conglomerates that are interbedded with mudstones. Although no trough cross-stratification was observed, the lack of fine-grained matrix and gravel-sand couplets indicate that these conglomerates and mudstones were most likely deposited in a gravel-bed dominated braided river depositional setting.

4.2. Magnetostratigraphy

4.2.1. Rock magnetics

Most samples have low magnetic susceptibility around $2.0*10^{-4}$ SI (International System of Units) but values up to 10^{-3} SI suggest a low contribution of magnetite in some samples (Supplementary Fig. S1). Isothermal remanent magnetization (IRM) acquisitions do not show saturation in high fields and thermal demagnetization of the IRMs indicates that hematite is the main remanent magnetic carrier in the samples of both sections (Supplementary Fig. S2). Stepwise thermal demagnetization confirms that the Characteristic Remanent Magnetization (ChRM) is carried by hematite with high unblocking temperatures (Fig. 4). Normal and reverse polarities are observed in both sections (Fig. 4). There is no difference in the magnetic properties of samples with normal or reverse polarities. The Khirmanjo section has steep to vertical bedding while the conglomerate layers at Shurabad are only slightly tilted (Fig. 1D). The ChRM directions cluster after bedding correction into antipodal NW down and SE up orientations reflecting normal and reversed directions, respectively (Fig. 4). ChRM directions thus pass both reversals and fold tests, suggesting they reflect primary magnetizations that have not been significantly affected by secondary overprints and are therefore suitable for magnetostratigraphic analysis.

4.2.2. Magnetostratigraphic analysis

Among the 533 paleomagnetic samples, 351 (66%) yielded reliable characteristic remanence (ChRM) directions. Polarity zones were defined by at least two consecutive samples with the same polarity. In total, there are 33 polarity zones identified with 16 normal zones (N1–N16; Fig. 5) and 17 reverse zones (R1–R17). The magnetostratigraphic section was constructed by correlating measured polarity zones with the Geomagnetic Time Scale (GTS; Ogg, 2012).

To aid polarity correlations with the GTS, we adopted the maximum depositional ages determined from detrital zircon fission-track (ZFT) ages from the nearby Dashtijum section (Chapman et al., 2019), which is ~14 km to the north of the Khirmanjo section (Fig. 1). Due to the typically poor lateral extent of fluvial beds, it is not straightforward to make bed-to-bed correlations between these sections. We used satellite imagery to trace the lateral extent of bedding, as shown in Fig. 1C. Additionally, as will be shown in section 5.1.1, strata of these sections can be correlated at the formation/member scale. In particular, the lower boundary of the Baldshuan Formation is easily distinguished from the underlying marine deposits based on the disappearance of marine carbonate rocks and green mudstones, and appearance of terrestrial red clastic rocks. We used the 27 ± 2 Ma ZFT maximum depositional age (MDA) for the detrital zircon sample at the base of the Dashtijum section (Chapman et al., 2019) to constrain the basal age of the Khirmanjo section. Similarly, the other ZFT ages from the Dashtijum section (Fig. 1) were used to further constrain the magnetostratigraphic ages on the formation/member scale.

To aid our exploration of potential polarity correlations, we applied the automated investigation procedure based on a Dynamic Time Warping algorithm to compute potential solutions (Lallier et al., 2013). This automated investigation method minimizes variations in sediment accumulation rates and major depositional hiatus. The resulting correlation solutions strongly depend on the provided time window of sediment deposition. We therefore first used the automated method to explore multiple potential correlation solutions giving different time windows (Supplementary Fig. S3) and then targeted and improved these correlations with detailed manual adjustments, as discussed below.

Using the automated correlation with no time constraint results in a correlation solution spanning 15 Ma to 2 Ma. If the time window is loosely set to 30–0 Ma time window based on the basal 27 ± 2 Ma ZFT MDA, the solution spans 10–1.2 Ma. However, these two correlations visually show obvious misfit upon polarity zones correlation to the GTS and can be easily discarded based on outside constraints. For example, both correlations fail in the upper part above the Chingou Formation with the >3 km thick Tavildara, Karanak, and Polizak formations deposited within only 2 or 1.2 Myrs, which would incur unrealistic high sedimentation rates of >1.5–2 km/Myrs. To avoid this, an upper 5 Ma bound was set for a 30–5 Ma time window yielding an automatic correlation from 28 Ma to 12 Ma. This generated correlation can be visually improved to between 26.0 and 13.3 Ma (Fig. 5). It is most satisfactory for the upper part (mostly Shurobod section) but in the lower part (mostly Khirmanjo section) several chrons are missed (e.g. C6AN.1n) or poorly represented suggesting variations in accumulation rates and depositional discontinuities. These misfits in the lower part of this correlation led to setting the time window to 24–5 Ma, which yielded a 21–8 Ma correlation. This generated correlation is found satisfactory throughout, after only a few modifications in the 21–13 Ma interval. The observed 33 polarity zones correlate to the major normal and reverse chrons between C4r.1r and C6r of the GTS, which results in depositional ages between 19.7 and 8.1 Ma for the measured Khirmanjo and Shurobod sections (Fig. 5). The few short chrons not well represented (e.g., C5B1n) can be attributed to short depositional hiatuses. Choosing between the 26.0-13.6 Ma and 19.7–8.1 Ma correlations remains, however, challenging.

Compared with the detrital zircon fission-track ages from the Dashtijum section (Fig. 1; Chapman et al., 2019), the 19.7–8.1 Ma correlation yields lag times of 5–7 Ma. The corresponding sediment accumulation rates agree with the depositional environment changes at ca. 13.5 Ma increasing from ca. 200 to 400 mm/kyr, and generally showing higher accumulation rates in conglomerates than in mudstones. By contrast, the 26.0–13.6 Ma correlation yields lag times of 2–4 Ma and requires a sudden shift from 200 m/Myr to very high (>1000 m/Myr) sediment accumulation rates at 16.0 Ma that does not correspond to a facies change and is sustained until the top of the studies section at 13.6 Ma.

Although the 26.0–13.6 Ma correlation cannot be excluded without additional age constraints, we favor the 19.7–8.1 Ma correlation on account of its better paleomagnetic polarity zone correlations to the GTS and more reasonable accumulation rates. In the following discussion, we therefore use the age constraint of 19.7–8.1 Ma. However, we emphasize that no matter which of the two correlations is correct, the tectonic event discussed below occurred during the middle–late Miocene, either since ~12 Ma (favored correlation) or since ~15.5 Ma (alternative correlation).

4.3. Detrital zircon U-Pb ages

The U-Pb age spectra of the seven detrital zircon samples show a distinct difference between the lower four (19.8–12.4 Ma) and upper three (11.8–9 Ma) samples in that the former four have a major Cenozoic age peak at ~40 Ma, which is lacking in the latter three (Fig. 6). Zircon grains from the upper three samples are all older than 200 Ma. All samples have grains with a range of ages >200 Ma.

4.4. Mudstone bulk-rock ε_{Nd} values

Generally, the ε_{Nd} values can be divided into three intervals (Fig. 7B): between 20 and 16.8 Ma, the ε_{Nd} values show a decreasing trend from -8.71 to -9.83; between 16 and 12 Ma, there is an increasing trend from -9.82 to -7.95; between 12 and 8 Ma, the ε_{Nd} values show an increased variability between -9.04 and -5.98 without any obvious temporal trends.

4.5. Stable oxygen and carbon isotopic values

Temporally, three main trends can be observed from the carbonate cement $\delta^{18}O$ values (Fig. 7C): 1) a decreasing trend from -11‰ to -12.3‰ from 20–17 Ma; 2) an increasing trend from -12.3‰ to -10.8‰ from 17–12 Ma; and 3) a general decreasing trend from -10.8‰ to -12.0‰ from 12–8 Ma, with a negative excursion between ~11 and 10 Ma. Similarly, the $\delta^{13}C$ values also show three trends (Fig. 7D): 1) a slightly increasing trend from -5.0‰ to -4.6‰ from 20–17 Ma; 2) a decreasing trend from -4.6‰ to -7.4‰ from 17–13.5 Ma; and 3) an increasing trend from -7.4‰ to -3.1‰ from 13.5–8 Ma. The $\delta^{18}O$ values of the three paleosol nodular carbonates are indistinguishable from those of carbonate cements in the bulk rock samples, while their $\delta^{13}C$ values are the most negative among all samples (Fig. 7C–D).

4.5.1. Evaluation of potential detrital carbonate contamination

Detrital carbonate grains are observed in some of the carbonate cemented sandstone samples (Fig. 8 and Table 2). We argue below that their influence is unlikely to be the dominant factor controlling the general isotopic trends (Fig. 7C–D) for the following reasons:

In the study area, potential sources of the detrital carbonate grains include Late Cretaceous–Eocene marine limestones (Kaya et al., 2019; Kaya et al., 2020) and Paleozoic limestones, both outcrop in the North Pamir (Klocke et al., 2017). The Late Cretaceous–Eocene limestones are not diagenetically altered (Kaya et al., 2019), and their average $\delta^{18}O$ and $\delta^{13}C$ values are -5‰ and 1‰, respectively (Bougeois et al., 2018), both of which are much higher than those of the carbonate cements of this study ($\delta^{18}O$: -10‰ to -14‰; $\delta^{13}C$: -2‰ to -9‰; Fig. 7C–D). If detrital carbonates from these Late Cretaceous–Eocene limestones were controlling the isotopic variations, the measured $\delta^{18}O$ and $\delta^{13}C$ values would show corresponding parallel trends, i.e., higher carbonate cement $\delta^{18}O$ values indicate more contribution of detrital carbonate grains, which would also cause higher $\delta^{13}C$ values. The opposing trends of the $\delta^{18}O$ and $\delta^{13}C$ values (Fig. 7C–D) indicate that this is unlikely the case.

For the Paleozoic limestones in the North Pamir, no stable isotopic values have been reported. If they were not diagenetically altered and the primary marine limestone stable isotopic values still hold, the above reasoning for the Cretaceous–Eocene limestones also applies. If they experienced diagenetic alteration during the Mesozoic tectonism and metamorphism and exhibit very low $\delta^{18}O$ values (e.g., lower than -14‰), the fact that samples with more negative $\delta^{18}O$ values (e.g., between 11 and 10 Ma) do not correspond to more detrital carbonate grains (Table 2) argues against their dominant influence.

4.5.2. Diagenesis screening

Our observations, as listed below, suggest that the carbonate cements of this study were most likely formed during early diagenesis when shallowly buried. First, petrographic observations show the appearance of fibrous calcite cement (Fig. 8C), which is a typical form of primary carbonate cement formed in the phreatic zone below the groundwater table (Kendall, 1985).

Second, cathodoluminescence observations indicate homogeneous luminescence for the carbonate cements (Fig. 8F), suggesting that the cement was formed in chemically similar water, with no influence of deep burial fluid. Third, the intergranular volume (IGV), which is between 34 and 62% in the investigated samples, does not show a systematic decrease throughout the stratigraphic section (Table 2). Considering >3 km of younger deposits lie above the Chingou and Baldshuan formations in the study area (Dedow et al., 2020), it is expected that the IGV would be lower than 15–20% (Baldwin & Butler, 1985). Thus, the observed high IGV values strongly suggest that cementation occurred during early diagenesis at shallow depths that prevented deep burial compaction (Paxton et al., 2002). Additional considerations support the inference of an early diagenetic origin for the carbonate cements: 1) the similarity of $\delta^{18}O$ values between the paleosol nodular carbonates and adjacent carbonate cements (Fig. 7C) indicates that the carbonate cements were precipitated in shallow groundwater, which has similar $\delta^{18}O$ values to the vadose zone soil water. 2) Deep burial diagenetic alteration is unlikely as this would lead to much lower $\delta^{18}O$ values in the lower part of the section compared to samples in the upper section due to higher burial temperatures (e.g., Garzione et al., 2004), which is not the case.

Based on the above observations, we conclude that the carbonate cements in our bulk samples most likely were precipitated during early diagenesis, and their $\delta^{18}O$ and $\delta^{13}C$ values reflect those of shallow groundwater, which was mainly recharged by surface water from the catchment. In contrast to humid regions where groundwater is recharged mainly by infiltration of local precipitation, in semiarid to arid environments, where precipitation is limited and the rate of evapotranspiration typically exceeds that of precipitation, the dominant recharge source is river water (Wilson & Guan, 2004; Markovich et al., 2019). The Miocene Tajik Basin was probably dominated by a semiarid to arid environment because of its intracontinental setting long after the retreat of the proto-Paratethys sea, as evidenced by the late Oligocene aeolian deposition in the central basin (Wang et al., 2019). River water as the dominant mechanism of recharge is typical for mountain front areas, such as the eastern Tajik Basin, where groundwater recharge is mainly through mountain front and mountain block recharges (Wilson & Guan, 2004; Markovich et al., 2019), which accumulate precipitation from the whole catchment in the high elevation mountains.

5. Discussion

5.1. Middle–late Miocene growth of the North Pamir

5.1.1. Middle Miocene Regional lithostratigraphic changes

In the Khirmanjo and Shurobod sections, the most prominent sedimentological change is observed around 13.5 Ma, marked by the transition from the fine-grained mudstone-dominated Childara Member to the coarse-grained conglomerate dominated Chingou Formation (Figs. 7 and 9). This lithofacies change is also accompanied by an increase in sediment accumulation rate from 194 m/Myr to 316 m/Myr (Fig. 7A), which we interpret to document a tectonic event. The occurrence of debris flow deposits with 1–2 m size angular boulders in the lower Shurobod section (Fig. 3E) indicates strong tectonic activity and/or high topography proximal to the depositional site.

The stratigraphy of the Khirmanjo & Shurobod sections can be correlated to several other sections in the north-eastern (e.g., Tavildara section) and eastern (e.g., Obi Khudkham and Dashtijum sections; Fig. 1) Tajik basin, based on member/formation scale lithofacies variations (Fig. 9). Sedimentary sections in the eastern Tajik Basin show similar lithofacies changes, such as the fine-grained Shurisay Member, to the conglomerate dominated Kamolin Member, to the fine-grained Childara Member, and then to the conglomerate dominated Chingou Formation (Fig. 9, Khirmanjo & Shurobod, Obi Khudkham, and Dashtijum sections) (Chapman et al., 2019; Dedow et al., 2020; this study). All three sections show a major lithofacies change from the fine-grained Childara Member to the coarse-grained Chingou Formation. Slightly different in the Tavildara section of the north-eastern Tajik Basin, rocks of the Baldshuan and Chingou formations are dominated by sandstones and siltstones, with limited appearance of conglomerates. However, the general lithofacies trends, i.e., fine-grained and coarse-grained cycles, remain apparent (Klocke et al., 2017) to enable correlation to other sections farther south in the eastern Tajik Basin (Fig. 9).

The newly dated ~13.5 Ma timing of this lithofacies change between the Childara Member and the Chingou Formation across the eastern and northeastern Tajik Basin suggests a middle Miocene phase of deformation propagation in the source terrane. The timing is also coeval with the initiation of thick conglomerate deposition and growth strata in the Tarim Basin starting ca. 15 Ma (Fig. 9) (Zheng et al., 2015; Blayney et al., 2019), which has been interpreted to denote deformation and thrusting of the North Pamir onto the Tarim Basin (Blayney et al., 2019). Together, this suggests a regional-scale deformation in the North Pamir starting in the late middle Miocene.

We noted that in the PE section of the central Tajik Basin, a previous magnetostratigraphic study reported depositional ages of 37.4–23.3 Ma for the Baldshuan (Shurisay, Kamolin, and Childara members) and Chingou formations, with a boundary age between these two at ~25 Ma (Wang et al., 2020), which is distinct from the ~13.5 Ma age reported in this study. We attribute this discrepancy to be a result of the loose lithostratigraphic usage of the formation and member names across the basin (e.g., Klocke et al., 2017).

5.1.2. Middle Miocene detrital source change

The disappearance of Eocene zircons around 12 Ma (Fig. 6) suggests a significant detrital source change. The potential source terranes for the eastern Tajik Basin include the North, Central, and South Pamir (Fig. 1 and Supplementary Fig. S4). The Southwest Tian Shan is not considered as a potential source as it only became a minor contributor to its foothill deposits since the Pliocene (Klocke et al., 2017).

The Vanj complex (45–35 Ma; Fig 10) of the Central Pamir (Fig. 1) is a potential source for the Eocene detrital zircons found in the lower four samples of our section, which were deposited between 20 and 12 Ma (Lukens et al., 2012; Chapman et al., 2018). By contrast, suitable source rocks for the Eocene grains have not been recorded in the North Pamir (Lukens et al., 2012; Chapman et al., 2017; Chapman et al., 2019; Li et al., 2020). The >200 Ma ages of these samples can either be sourced from the Mesozoic strata surrounding these Eocene granitoids in the Central Pamir or from the exposed North Pamir (Fig.10). In contrast, the upper three samples that are between 12 and 8 Ma lack the Eocene age peak at 40 Ma (Fig. 10), indicating the disappearance of detritus from the Central Pamir; while the exclusively >200 Ma ages are consistent with a dominant detrital source in the North Pamir. Interestingly, a similar disappearance of ~40 Ma detrital zircon ages was also observed in the Oytag section in western Tarim Basin (Fig. 1A), the timing of which is only poorly constrained to be post-early Miocene (Bershaw et al., 2012).

The inferred provenance change at ~12 Ma is also supported by mudstone bulk-rock ε_{Nd} values which become less negative and more variable after 12 Ma (Fig. 7B). The change from more negative to less negative ε_{Nd} values seems to agree with the change of provenance from the Central (ε_{Nd} values: -7.7 and -9.6) to the North Pamir (ε_{Nd} values: -6.4 and -9.9) (Blayney et al., 2016; Blayney et al., 2019) as inferred from detrital zircon U-Pb data. We note however that the uncertainties in this inference are high because modern river mud ε_{Nd} data used to characterize the Central and North Pamir are sparse and from the eastern rather than western Pamir and therefore may not be representative. Regardless, the ε_{Nd} signatures clearly support the inference that a significant provenance shift occurred around 12 Ma.

In the nearby Dashtijum section, detrital zircon U-Pb ages have been reported from five sandstone samples collected from the Baldshuan, Chingou, and Tavildara formations, all of which show a prominent Eocene age peak (Fig. 10; Chapman et al., 2019). This is different from the detrital zircon U-Pb age spectra of samples from the Khirmanjo and Shurobod sections, in which the upper three samples of the Chingou Formation do not have Eocene zircons. We interpret this difference to result from the different stratigraphic intervals sampled in the different studies. The lower four samples of the Dashtijum section can be correlated to the 20–12 Ma interval of the Khirmanjo section, i.e., Baldshuan and lower Chingou formations (Fig. 1), which share very similar U-Pb age spectra (Fig. 10). A 1500-meter sampling gap separates these samples from the top one sample of the Dashtijum section assigned to the Tavildara Formation (Chapman et al., 2019) and correlated stratigraphically above the Shurobod section. We thus interpret that the interval in which we have recorded the disappearance of Eocene detrital zircons lies in the correlative 1500 m sampling gap in the Dashtijum section (Figs. 1C and 10). This implies that Eocene detrital zircons were recorded since the late Eocene, then disappeared at ca. 12 Ma and reappeared after 8 M, according to our favored magnetostratigraphic correlation.

5.1.3. Middle–late Miocene stable isotopic shifts

The provenance shift at ~12 Ma also appears to correspond to a change in the $\delta^{18}O$ values of carbonate cement in our bulk mudstone and sandstone samples. The $\delta^{18}O$ values generally show a negative shift starting from ~12 Ma to the top of the section but with a negative excursion between 11 and 10 Ma (Fig. 7C; see Supplementary Text S5 for a detailed discussion of the excursion). Concurrently, the $\delta^{13}C$ values show a constant gradual positive shift (Fig. 7D).

For the negative shift of the $\delta^{18}O$ values, several potential causes are explored: global climate cooling, moisture source change, as well as surface uplift. Global cooling can influence $\delta^{18}O$ values in two opposing ways: temperature decrease can cause the decrease of $\delta^{18}O$ values of precipitation while the increase of $\delta^{18}O$ values of carbonate with a combined effect of 0.36‰/°C (Kim & O'Neil, 1997). During the Miocene, there is a significant global climate cooling step after the mid-Miocene Climate Optimum at ~14 Ma (Westerhold et al., 2020); this step is very different from the gradual decreasing trend we observe, starting at ~12 Ma (or 15.5 Ma in the alternative correlation).

Currently, the Tajik Basin moisture source is dominated by the Westerlies and this pattern is generally confirmed to have prevailed since the Eocene by regional stable isotopic studies (e.g., Caves et al., 2015; Bougeois et al., 2018), as well as climate modeling (e.g., Tardif et al., 2020; Wang et al., 2020). We thus also exclude moisture source change as a potential driving factor of the isotopic change.

The remaining potential driver of the negative shift of $\delta^{18}O$ values in our sedimentary succession is surface uplift enhancing Rayleigh distillation during the forced orographic ascension of water vapor (Rowley & Garzione, 2007). As previously proposed, surface uplift may have increased the amount of orographic precipitation and also enhanced the precipitation seasonality with increasing winter precipitation (Sha et al., 2018); both of these processes can lead to negative shifts of $\delta^{18}O$ values due to decreased sub-cloud evaporation (Li & Garzione, 2017) and lower precipitation temperature, respectively (Caves et al., 2017; Bershaw & Lechler, 2019).

Similarly, the associated positive shift of the $\delta^{13}C$ values (Fig. 7D) is more likely explained by surface uplift than other potential drivers, such as the appearance of C4 plants or addition of marine carbonate dissolution. First, C4 plant expansion is unlikely the major driver as it occurred only later near the Miocene–Pliocene boundary in broad areas of Central Asia (Shen et al., 2018) or Quaternary in the Tajik Basin (Yang & Ding, 2006). Although the potential influence of marine carbonate dissolution cannot be excluded, the fact that the $\delta^{13}C$ values increased in a constantly gradual way that is also in concert with the $\delta^{18}O$ values, suggests that progressive surface uplift is probably the dominant cause, rather than marine carbonate dissolution, in which case a more abrupt shift and decoupling with oxygen shift would be expected. Indeed, surface uplift can explain the increase of the $\delta^{13}C$ values through two independent mechanisms: first, the decreased photosynthetic discrimination of plants under lower atmosphere $p(CO_2)$ due to higher elevations would increase the $\delta^{13}C$ values of plants (Körner et al., 1991); second, soil respiration rate would decrease with lower temperatures (Lloyd & Taylor, 1994) associated with higher elevations (Cerling & Quade, 1993). Both mechanisms could have increased the $\delta^{13}C$ values of the soil CO_2, which would dissolve in waters and contribute to the dissolved inorganic carbon pool of the shallow groundwater in the basin through mountain-front recharge (Wilson & Guan, 2004; Markovich et al., 2019).

Although we acknowledge there may be other potential causes for the stable oxygen and carbon isotopic changes, the close correspondence with the timing of tectonic deformation in the source terranes inferred from lithofacies and provenance evidence leads us to interpret these stable isotopic shifts to most likely reflect surface uplift of the source terrane (i.e., the North Pamir). This interpretation of stable isotopes agrees with previous interpretations of similar negative shifts of stable oxygen isotopic trends in Central Asia, such as in the PE section within the Tajik basin at 25 Ma (Wang et al., 2020) and several other sections farther north on the windward side of the Tian Shan (Rugenstein & Chamberlain, 2018).

5.2 Broader implications

Based on the above discussed multiple sets of evidence, we interpret our data to suggest that around 13.5 Ma, thrusting in the Pamir propagated towards the foreland causing the significant lithofacies change and accumulation rate increase. At ~12 Ma, continued deformation and foreland-ward propagation of the fold-thrust belt may explain the cutting-off of the Central Pamir detrital source and a confined provenance in the North Pamir (ending after 8 Ma potentially because the river headwater incised back into the Central Pamir). The more variable ε_{Nd} values after 12 Ma probably reflect shifting drainages within the North Pamir in response to ongoing foreland-ward propagation of the fold-thrust belt.

Middle–late Miocene North Pamir deformation recorded in adjacent basins is consistent with late Miocene exhumation ages from thrust sheets associated with the deformation of the Tajik Basin (Chapman et al., 2017; Abdulhameed et al., 2020) as well as north-western Pamir exhumation from apatite fission-track ages between 10.3 Ma and 6.2 Ma (Abdulhameed et al., 2020).

In addition to the middle–late Miocene phase of growth recorded in this and previous studies (Klocke et al., 2017; Chapman et al., 2019; Dedow et al., 2020), an earlier late Oligocene–early Miocene growth phase of the Pamir has also been documented (Coutand et al., 2002; Amidon & Hynek, 2010; Wang et al., 2019; Wang et al., 2020). These two deformation phases are also well-documented in the Tarim Basin sedimentary records (Zheng et al., 2015; Blayney et al., 2019), as well as in Tien Shan thermochronology data (Hendrix et al., 1994; Sobel & Dumitru, 1997; Dumitru et al., 2001; Sobel et al., 2013). The record of these two phases of deformation over a broad area suggests a regional mechanism.

Deformation of the North Pamir since ~15–12 Ma is concurrent with 1) the tectonic regime shift from extensional to contractional deformation in the Central Pamir at ~12–10 Ma (Rutte et al., 2017), 2) internal deformation of the Tajik Basin since ~12 Ma (Chapman et al., 2017; Abdulhameed et al., 2020), and 3) rapid exhumation of the Southwest Tian Shan since ~12–10 Ma (Jepson et al., 2018; Abdulhameed et al., 2020). These observations agree with the proposal that resumed northward underthrusting of the Indian lower crust and mantle lithosphere, after the 25–20 Ma slab retreat and breakoff (Mahéo et al., 2002; DeCelles et al., 2011), forced the delamination of the cratonic Asian mantle lithosphere since ~12–10 Ma (Kufner et al., 2016; Rutte et al., 2017), which caused synchronous deformation in the North Pamir, Tajik and Tarim basins and southwest Tian Shan. Note that the forced delamination was inferred by Kufner et al. (2016) based on the comparing lengths of an ~380 km long slow anomaly thought to be delaminated Asian mantle lithosphere beneath the Pamir with similar northward underthrusting of the Indian mantle lithosphere since ~12–10 Ma.

Middle to late Miocene deformation in the North Pamir and associated surface uplift may relate to coeval regional climate changes. Topographic growth of the Pamir mountains deflecting the Westerly moisture is invoked for enhanced aridity in the leeward (Tarim) side while increasing orographic precipitation in the windward (Tajik) side (e.g., Caves et al., 2015). Previous studies interpreted the late Oligocene–early Miocene appearance of eolian deposits in the Tarim Basin (Zheng et al., 2015) and coeval wetting signals in the Tajik basin (Wang et al., 2020) that fit well with the Pamir-Tian Shan deformation reported at this time (Sun et al., 2010; Qiang et al., 2011; Zheng et al., 2015). However, a pronounced late middle Miocene to Pliocene aridification is also reported from Tarim (e.g., Heermance et al., 2013; Liu et al., 2014; Bougeois et al., 2018; Heermance et al., 2018) and farther east into the Qaidam Basin and beyond (Dettman et al., 2003;

Zhuang et al., 2011; Li et al., 2016) based on positive carbonate $\delta^{18}O$ shifts combined with sedimentological proxies. These latter aridification events have also been interpreted to reflect the topographic growth of the Pamir and Tian Shan, which is supported by results of this study, although global climate cooling and increased variability since the middle Miocene Climate Optimum (17–14 Ma) probably also contributed to the aridification (Barbolini et al., 2020).

6. Conclusions

This study measured and dated a new sedimentary section in the eastern Tajik Basin. Magnetostratigraphic study indicates that the Baldshuan and Chingou formations were deposited from 20–8 Ma. A prominent lithofacies change from fine-grained floodplain-dominated braided river facies to a coarse-grained braided river channel and alluvial fan-dominated depositional setting occurred around 13.5 Ma. Detrital zircon U-Pb zircon age spectra and mudstone bulk-rock ε_{Nd} values indicate a sediment source change from the Central Pamir to the North Pamir at ~12 Ma. Accompanied with the provenance change, stable oxygen and carbon isotopic values derived from carbonate cement bearing mudstones and sandstones show decreasing and increasing trends respectively after 12 Ma, which are interpreted to reflect surface uplift of the drainage basin. Integrating these lines of evidence from the new section with previous studies from both the Tajik and Tarim basins, we suggest deformation propagation and surface uplift of the North Pamir during the middle to late Miocene. Our results agree with models that predict delamination since 12–10 Ma with associated late Miocene deformation of the North Pamir and surrounding regions. Results of this study, when combined with previous work, emphasize that the Pamir experienced multiple phases of deformation and topographic growth during the late Paleogene–Neogene to form its present height and arcuate shape.

Acknowledgments

We would like to thank Pierrick Roperch for help with paleomagnetic analysis and data processing; Niklas Löffler and Penny Higgins for help with carbonate cement stable isotopes analysis; Mauricio Ibanez Meijer, Jacob Buettner, and Yanling Wang for help with detrital zircon U-Pb analyses; David Vilbert for help with neodymium isotopic analysis. We would like to thank Alexander Robinson, John Bershaw, and an anonymous reviewer for helpful comments, and Jones Kley, Thomas Voigt, James Chapman, Peter DeCelles, and Edward Sobel for comments on earlier versions. This project is supported by the European Research Council consolidator grant MAGIC 649081 to GDN.

References

Abdulhameed, S., Ratschbacher, L., Jonckheere, R., Gągała, Ł., Enkelmann, E., Käßner, A., et al. (2020). Tajik Basin and Southwestern Tian Shan, Northwestern India-Asia Collision Zone: 2. Timing of Basin Inversion, Tian Shan Mountain Building, and Relation to Pamir-Plateau Advance and Deep India-Asia Indentation. *Tectonics, 39, doi: 10.1029/2019TC005873*.

Amidon, W. H., & Hynek, S. A. (2010). Exhumational history of the north central Pamir. *Tectonics, 29, doi:10.1029/2009TC002589*.

Aminov, J., Ding, L., Mamadjonov, Y., Dupont-Nivet, G., Aminov, J., Zhang, L.-Y., et al. (2017). Pamir Plateau formation and crustal thickening before the India-Asia collision inferred from dating and petrology of the 110–92 Ma Southern Pamir volcanic sequence. *Gondwana Research, 51*, 310-326.

Angiolini, L., Zanchi, A., Zanchetta, S., Nicora, A., & Vezzoli, G. (2013). The Cimmerian geopuzzle: new data from South Pamir. *Terra Nova, 25*(5), 352-360.

Baldwin, B., & Butler, C. O. (1985). Compaction curves. *AAPG Bulletin, 69*(4), 622-626.

Barbolini, N., Woutersen, A., Dupont-Nivet, G., Silvestro, D., Tardif, D., Meijer, N., et al. (2020). Cenozoic evolution of the steppe-desert biome in Central Asia. *Science Advances, 6*(41), eabb8227.

Bershaw, J., Garzione, C. N., Schoenbohm, L., Gehrels, G., & Tao, L. (2012). Cenozoic evolution of the Pamir plateau based on stratigraphy, zircon provenance, and stable isotopes of foreland basin sediments at Oytag (Wuyitake) in the Tarim Basin (west China). *Journal of Asian Earth Sciences, 44*, 136-148.

Bershaw, J., & Lechler, A. R. (2019). The isotopic composition of meteoric water along altitudinal transects in the Tian Shan of Central Asia. *Chemical Geology, 516*, 68-78.

Blayney, T., Dupont-Nivet, G., Najman, Y., Proust, J. N., Meijer, N., Roperch, P., et al. (2019). Tectonic evolution of the Pamir recorded in the western Tarim Basin (China): sedimentologic and magnetostratigraphic analyses of the Aertashi section. *Tectonics, 38, doi: 10.1029/2018TC005146*.

Blayney, T., Najman, Y., Dupont-Nivet, G., Carter, A., Millar, I., Garzanti, E., et al. (2016). Indentation of the Pamirs with respect to the northern margin of Tibet: Constraints from the Tarim basin sedimentary record. *Tectonics, 35*(10), 2345-2369.

Bougeois, L., Dupont-Nivet, G., de Rafélis, M., Tindall, J. C., Proust, J.-N., Reichart, G.-J., et al. (2018). Asian monsoons and aridification response to Paleogene sea retreat and Neogene westerly shielding indicated by seasonality in Paratethys oysters. *Earth and Planetary Science Letters, 485*, 99-110.

Burtman, V. S., & Molnar, P. H. (1993). *Geological and geophysical evidence for deep subduction of continental crust beneath the Pamir*: Geological Society of America special publication, 281, doi: 10.1130/SPE281-p1.

Carrapa, B., DeCelles, P. G., Wang, X., Clementz, M. T., Mancin, N., Stoica, M., et al. (2015). Tectono-climatic implications of Eocene Paratethys regression in the Tajik basin of central Asia. *Earth and Planetary Science Letters, 424*, 168-178.

Carrapa, B., Mustapha, F. S., Cosca, M., Gehrels, G., Schoenbohm, L. M., Sobel, E. R., et al. (2014). Multisystem dating of modern river detritus from Tajikistan and China: Implications for crustal evolution and exhumation of the Pamir. *Lithosphere, 6*(6), 443-455.

Caves, J. K., Bayshashov, B. U., Zhamangara, A., Ritch, A. J., Ibarra, D. E., Sjostrom, D. J., et al. (2017). Late Miocene Uplift of the Tian Shan and Altai and Reorganization of Central Asia Climate. *GSA today, 27, doi: 10.1130/GSATG305A.1.*

Caves, J. K., Winnick, M. J., Graham, S. A., Sjostrom, D. J., Mulch, A., & Chamberlain, C. P. (2015). Role of the westerlies in Central Asia climate over the Cenozoic. *Earth and Planetary Science Letters, 428*, 33-43.

Cerling, T. E., & Quade, J. (1993). Stable carbon and oxygen isotopes in soil carbonates. *Geophysical Monograpy, 78*, 217-231.

Chapman, J. B., Carrapa, B., Ballato, P., DeCelles, P. G., Worthington, J., Oimahmadov, I., et al. (2017). Intracontinental subduction beneath the Pamir Mountains: Constraints from thermokinematic modeling of shortening in the Tajik fold-and-thrust belt. *GSA Bulletin, 129*(11-12), 1450-1471.

Chapman, J. B., Carrapa, B., DeCelles, P. G., Worthington, J., Mancin, N., Cobianchi, M., et al. (2019). The Tajik Basin: a composite record of sedimentary basin evolution in response to tectonics in the Pamir. *Basin Research, doi: 10.1111/bre.12381*.

Chapman, J. B., Scoggin, S. H., Kapp, P., Carrapa, B., Ducea, M. N., Worthington, J., et al. (2018). Mesozoic to Cenozoic magmatic history of the Pamir. *Earth and Planetary Science Letters, 482*, 181-192.

Chen, X., Chen, H., Lin, X., Cheng, X., Yang, R., Ding, W., et al. (2018). Arcuate Pamir in the Paleogene? Insights from a review of stratigraphy and sedimentology of the basin fills in the foreland of NE Chinese Pamir, western Tarim Basin. *Earth-Science Reviews, 180*, 1-16.

Coutand, I., Strecker, M., Arrowsmith, J., Hilley, G., Thiede, R., Korjenkov, A., & Omuraliev, M. (2002). Late Cenozoic tectonic development of the intramontane Alai Valley,(Pamir-Tien Shan region, central Asia): An example of intracontinental deformation due to the Indo-Eurasia collision. *Tectonics, 21*(6).

DeCelles, P., Kapp, P., Quade, J., & Gehrels, G. (2011). Oligocene–Miocene Kailas basin, southwestern Tibet: Record of postcollisional upper-plate extension in the Indus-Yarlung suture zone. *Geological Society of America Bulletin, 123*(7-8), 1337-1362.

Dedow, R., Franz, M., Szulc, A., Schneider, J. W., Brückner, J., Ratschbacher, L., et al. (2020). Tajik Basin and Southwestern Tian Shan, Northwestern India-Asia Collision Zone: 3. Pre- to Syn-orogenic Retro-foreland Basin Evolution in the Eastern Tajik Depression and Linkage to the Pamir Hinterland. *Tectonics, 38, doi: 10.1029/2019TC005874*.

Dettman, D. L., Fang, X., Garzione, C. N., & Li, J. (2003). Uplift-driven climate change at 12 Ma: a long δ18O record from the NE margin of the Tibetan plateau. *Earth and Planetary Science Letters, 214*(1-2), 267-277.

Dumitru, T. A., Zhou, D., Chang, E. Z., Graham, S. A., Hendrix, M. S., Sobel, E. R., & Carroll, A. R. (2001). Uplift, exhumation, and deformation in the Chinese Tian Shan. *Geological Society of America Memoir, 194*, 71-99.

Garzione, C. N., Dettman, D. L., & Horton, B. K. (2004). Carbonate oxygen isotope paleoaltimetry: evaluating the effect of diagenesis on paleoelevation estimates for the Tibetan plateau. *Palaeogeography, Palaeoclimatology, Palaeoecology, 212*(1-2), 119-140.

He, J., Kapp, P., Chapman, J. B., DeCelles, P. G., & Carrapa, B. (2018). Structural setting and detrital zircon U–Pb geochronology of Triassic–Cenozoic strata in the eastern Central Pamir, Tajikistan. *Geological Society, London, Special Publications, 483*, SP483. 411.

Heermance, R. V., Pearson, J., Moe, A., Langtao, L., Jianhong, X., Jie, C., et al. (2018). Erg deposition and development of the ancestral Taklimakan Desert (western China) between 12.2 and 7.0 Ma. *Geology, 46*(10), 919-922.

Heermance, R. V., Pullen, A., Kapp, P., Garzione, C. N., Bogue, S., Ding, L., & Song, P. P. (2013). Sedimentological and stable isotopic evidence for inversion of the Qaidam Basin, China, associated with climate change during the Plio-Quaternary transition. *Geological Society of America Bulletin, 125*(5-6), 833-856.

Hendrix, M. S., Dumitru, T. A., & Graham, S. A. (1994). Late Oligocene-early Miocene unroofing in the Chinese Tian Shan: An early effect of the India-Asia collision. *Geology, 22*(6), 487-490.

Jepson, G., Glorie, S., Konopelko, D., Gillespie, J., Danišík, M., Evans, N. J., et al. (2018). Thermochronological insights into the structural contact between the Tian Shan and Pamirs, Tajikistan. *Terra Nova, 30*(2), 95-104.

Kaya, M. Y., Dupont-Nivet, G., Proust, J. N., Roperch, P., Bougeois, L., Meijer, N., et al. (2019). Paleogene evolution and demise of the proto-Paratethys Sea in Central Asia (Tarim and Tajik basins): role of intensified tectonic activity at~ 41 Ma. *Basin Research, doi:10.1111/bre.12330*.

Kaya, M. Y., Dupont-Nivet, G., Proust, J. N., Roperch, P., Meijer, N., Frieling, J., et al. (2020). Cretaceous Evolution of the Central Asian Proto-Paratethys Sea: Tectonic, Eustatic, and Climatic Controls. *Tectonics, 39, doi.org/10.1029/2019TC005983*.

Kendall, A. C. (1985). Radiaxial fibrous calcite: a reappraisal. In N. Schneidermann & P. M. Harris (Eds.), *Carbonate Cements* (pp. 59-77): Special Publications of SEPM.

Kim, S. T., & O'Neil, J. R. (1997). Equilibrium and nonequilibrium oxygen isotope effects in synthetic carbonates. *Geochimica et Cosmochimica Acta, 61*(16), 3461-3475.

Klocke, M., Voigt, T., Kley, J., Pfeifer, S., Rocktäschel, T., Keil, S., & Gaupp, R. (2017). Cenozoic evolution of the Pamir and Tien Shan Mountains reflected in syntectonic deposits of the Tajik Basin. *Geological Society, London, Special Publications, 427*(1), 523-564.

Körner, C., Farquhar, G. D., & Wong, S. C. (1991). Carbon isotope discrimination by plants follows latitudinal and altitudinal trends. *Oecologia, 88*(1), 30-40.

Kufner, S.-K., Schurr, B., Sippl, C., Yuan, X., Ratschbacher, L., Ischuk, A., et al. (2016). Deep India meets deep Asia: Lithospheric indentation, delamination and break-off under Pamir and Hindu Kush (Central Asia). *Earth and Planetary Science Letters, 435*, 171-184.

Lallier, F., Antoine, C., Charreau, J., Caumon, G., & Ruiu, J. (2013). Management of ambiguities in magnetostratigraphic correlation. *Earth and Planetary Science Letters, 371*, 26-36.

Li, L., & Garzione, C. N. (2017). Spatial distribution and controlling factors of stable isotopes in meteoric waters on the Tibetan Plateau: Implications for paleoelevation reconstruction. *Earth and Planetary Science Letters, 460*, 302-314.

Li, L., Garzione, C. N., Pullen, A., & Chang, H. (2016). Early–middle Miocene topographic growth of the northern Tibetan Plateau: Stable isotope and sedimentation evidence from the southwestern Qaidam basin. *Palaeogeography, Palaeoclimatology, Palaeoecology, 461*, 201-213.

Li, Y. P., Robinson, A., Gadoev, M., & Oimuhammadzoda, I. (2020). Was the Pamir salient built along a Late Paleozoic embayment on the southern Asian margin? *Earth and Planetary Science Letters, 550, https://doi.org/10.1016/j.epsl.2020.116554*.

Liu, W., Liu, Z., An, Z., Sun, J., Chang, H., Wang, N., et al. (2014). Late Miocene episodic lakes in the arid Tarim Basin, western China. *Proceedings of the National Academy of Sciences, 111*(46), 16292-16296.

Lloyd, J., & Taylor, J. A. (1994). On the temperature dependence of soil respiration. *Functional ecology, 8*, 315-323.

Lukens, C., Carrapa, B., Singer, B., & Gehrels, G. (2012). Miocene exhumation of the Pamir revealed by detrital geothermochronology of Tajik rivers. *Tectonics, 31, doi:10.1029/2011TC003040*.

Mahéo, G., Guillot, S., Blichert-Toft, J., Rolland, Y., & Pêcher, A. (2002). A slab breakoff model for the Neogene thermal evolution of South Karakorum and South Tibet. *Earth and Planetary Science Letters, 195*(1), 45-58.

Markovich, K. H., Manning, A. H., Condon, L. E., & McIntosh, J. C. (2019). Mountain-block recharge: A review of current understanding. *Water Resources Research, 55*(11), 8278-8304.

Ogg, J. G. (2012). Geomagnetic Polarity Time Scale. In F. M. Gradstein, J. G. Ogg, M. Schmitz, & G. Ogg (Eds.), *The Geological Time Scale 2012* (pp. 85-113). Amsterdam: Elsevier.

Qiang, X. K., An, Z. S., Song, Y. G., Chang, H., Sun, Y., Liu, W., et al. (2011). New eolian red clay sequence on the western Chinese Loess Plateau linked to onset of Asian desertification about 25 Ma ago. *SCIENCE CHINA Earth Sciences, 54*(1), 136-144.

Rembe, J., Sobel, E. R., Kley, J., Zhou, R., Thiede, R., & Chen, J. (2021). The Carboniferous Arc of the North Pamir. *Lithosphere, 2021*(1), 6697858.

Robinson, A. C., Yin, A., Manning, C. E., Harrison, T. M., Zhang, S.-H., & Wang, X.-F. (2004). Tectonic evolution of the northeastern Pamir: Constraints from the northern portion of the Cenozoic Kongur Shan extensional system, western China. *Geological Society of America Bulletin, 116*(7-8), 953-973.

Rowley, D. B., & Garzione, C. N. (2007). Stable isotope-based paleoaltimetry. *Annual Review of Earth and Planetary Sciences, 35*, 463-508.

Rugenstein, J. K. C., & Chamberlain, P. (2018). The evolution of hydroclimate in Asia over the Cenozoic: A stable-isotope perspective. *Earth-Science Reviews, 185*, 1129-1156.

Rutte, D., Ratschbacher, L., Khan, J., Stübner, K., Hacker, B. R., Stearns, M. A., et al. (2017). Building the Pamir-Tibetan Plateau—Crustal stacking, extensional collapse, and lateral extrusion in the Central Pamir: 2. Timing and rates. *Tectonics, 36*(3), 385-419.

Schwab, M., Ratschbacher, L., Siebel, W., McWilliams, M., Minaev, V., Lutkov, V., et al. (2004). Assembly of the Pamirs: Age and origin of magmatic belts from the southern Tien Shan to the southern Pamirs and their relation to Tibet. *Tectonics, 23, doi:10.1029/2003TC001583*.

Sha, Y., Shi, Z., Liu, X., An, Z., Li, X., & Chang, H. (2018). Role of the Tian Shan Mountains and Pamir Plateau in increasing spatiotemporal differentiation of precipitation over interior Asia. *Journal of Climate, 31*(19), 8141-8162.

Shen, X., Wan, S., Colin, C., Tada, R., Shi, X., Pei, W., et al. (2018). Increased seasonality and aridity drove the C4 plant expansion in Central Asia since the Miocene–Pliocene boundary. *Earth and Planetary Science Letters, 502*, 74-83.

Sobel, E. R., Chen, J., Schoenbohm, L. M., Thiede, R., Stockli, D. F., Sudo, M., & Strecker, M. R. (2013). Oceanic-style subduction controls late Cenozoic deformation of the Northern Pamir orogen. *Earth and Planetary Science Letters, 363*, 204-218.

Sobel, E. R., & Dumitru, T. A. (1997). Thrusting and exhumation around the margins of the western Tarim basin during the India-Asia collision. *Journal of Geophysical Research, 102*(B3), 5043-5063.

Stübner, K., Ratschbacher, L., Weise, C., Chow, J., Hofmann, J., Khan, J., et al. (2013). The giant Shakhdara migmatitic gneiss dome, Pamir, India-Asia collision zone: 2. Timing of dome formation. *Tectonics, 32*(5), 1404-1431.

Sun, H., Chen, Y., Li, W., Li, F., Chen, Y., Hao, X., & Yang, Y. (2010). Variation and abrupt change of climate in Ili River Basin, Xinjiang. *Journal of Geographical Sciences, 20*(5), 652-666.

Sun, J., Xiao, W., Windley, B. F., Ji, W., Fu, B., Wang, J., & Jin, C. (2016). Provenance change of sediment input in the northeastern foreland of Pamir related to collision of the Indian plate with the Kohistan-Ladakh arc at around 47 Ma. *Tectonics, 35, doi:10.1002/ 2015TC003974.*

Sun, J., Zhang, Z., Cao, M., Windley, B. F., Tian, S., Sha, J., et al. (2020). Timing of seawater retreat from proto-Paratethys, sedimentary provenance, and tectonic rotations in the late Eocene-early Oligocene in the Tajik Basin, Central Asia. *Palaeogeography, Palaeoclimatology, Palaeoecology, 545, doi.org/10.1016/j.palaeo.2020.109657*.

Sun, J. M., & Jiang, M. S. (2013). Eocene seawater retreat from the southwest Tarim Basin and implications for early Cenozoic tectonic evolution in the Pamir Plateau. *Tectonophysics, 588*, 27-38.

Tardif, D., Fluteau, F., Donnadieu, Y., Le Hir, G., Ladant, J.-B., Sepulchre, P., et al. (2020). The origin of Asian monsoons: a modelling perspective. *Climate of the Past, 16*(3), 847-865.

Valet, J.-P., Fournier, A., Courtillot, V., & Herrero-Bervera, E. (2012). Dynamical similarity of geomagnetic field reversals. *Nature, 490*(7418), 89-93.

Villarreal, D. P., Robinson, A. C., Carrapa, B., Worthington, J., Chapman, J. B., Oimahmadov, I., et al. (2020). Evidence for Late Triassic crustal suturing of the Central and Southern Pamir. *Journal of Asian Earth Sciences: X, 3, doi.org/10.1016/j.jaesx.2019.100024*.

Wang, X., Carrapa, B., Chapman, J. B., Henriquez, S., Wang, M., Decelles, P. G., et al. (2019). Parathethys last gasp in central Asia and late Oligocene accelerated uplift of the Pamirs. *Geophysical Research Letters, 46, doi: https://doi.org/10.1029/2019GL084838*.

Wang, X., Carrapa, B., Sun, Y. C., Dettman, D. L., Chapman, J. B., & Rugenstein, J. K. C. (2020). The role of the westerlies and orography in Asian hydroclimate since the late Oligocene. *Geology, 48*(7), 728-732.

Westerhold, T., Marwan, N., Drury, A. J., Liebrand, D., Agnini, C., Anagnostou, E., et al. (2020). An astronomically dated record of Earth's climate and its predictability over the last 66 million years. *Science, 369*(6509), 1383-1387.

Wilson, J. L., & Guan, H. (2004). Mountain-block hydrology and mountain-front recharge. *Groundwater recharge in a desert environment: The Southwestern United States, 9*.

Worthington, J. R., Ratschbacher, L., Stübner, K., Khan, J., Malz, N., Schneider, S., et al. (2020). The Alichur dome, South Pamir, western India–Asia collisional zone: detailing the Neogene Shakhdara–Alichur syn-collisional gneiss-dome complex and connection to lithospheric processes. *Tectonics, 39, doi: 10.1029/2019TC005735*.

Yang, S., & Ding, Z. (2006). Winter–spring precipitation as the principal control on predominance of C3 plants in Central Asia over the past 1.77 Myr: evidence from δ13C of loess organic matter in Tajikistan. *Palaeogeography, Palaeoclimatology, Palaeoecology, 235*(4), 330-339.

Yin, A., & Harrison, T. M. (2000). Geologic evolution of the Himalayan-Tibetan orogen. *Annual Review of Earth and Planetary Sciences, 28*(1), 211-280.

Zheng, H. B., Wei, X. C., Tada, R., Clift, P. D., Wang, B., Jourdan, F., et al. (2015). Late oligocene–early miocene birth of the Taklimakan Desert. *Proceedings of the National Academy of Sciences, 112*(25), 7662-7667.

Zhuang, G. S., Hourigan, J. K., Koch, P. L., Ritts, B. D., & Kent-Corson, M. L. (2011). Isotopic constraints on intensified aridity in Central Asia around 12Ma. *Earth and Planetary Science Letters, 312*(1-2), 152-163.

Figure captions

Figure 1. (A) Simplified tectonic map of the Pamir and surrounding regions, showing major terranes, suture zones (black lines), faults (red lines), and gneiss domes (brown patches). Blue and yellow stars are modern river mud ε_{Nd} samples from the North and Central/South Pamir, respectively (Blayney et al., 2016; Blayney et al., 2019). Blue lines represent the Panj River system. Yellow circles are previously studied sections: PE, Carrapa et al. (2015) and Wang et al. (2019); TA (Tavildara), Klocke et al. (2017); Aksu, Sun et al. (2020); Aertashi, Zheng et al. (2015), Blayney et al. (2016) and Blayney et al. (2019); Oytag, Bershaw et al. (2012); KYTS, Kashgar-Yecheng transfer system; MPT, Main Pamir Thrust; RPS, Rushan-Pshart suture; TS, Taymas suture; TBZ, Tirich-Mir boundary zone. Inset: The dashed box shows the location of the main figure, Tajik Basin; HK, Hindu Kush. **(B)** Geologic map of the study area, adapted from Dedow et al. (2020). Black solid curves are measured sections of this study: KH, Khirmanjo section; SB, Shurobod section. Black dashed curves are previously studied sections: DH, Dashtijum section, Chapman et al. (2019); OK, Obi Khudkham section, Dedow et al. (2020). The dotted line correlates similar stratigraphic heights between the SB and KH sections. Filled circles represent detrital samples for geochronology and thermochronology studies of this study and Chapman et al. (2019): the blue, orange, and yellow colors represent different ages, e.g., 20–12 Ma, 12–8 Ma, and <8 Ma. Note that ages in the DH section are the younger age population derived from the kernel density estimates (KDE) curves of detrital zircon fission-track (ZFT) data. **(C)** Satellite image of the same area as (A). The rose-red solid (more reliable) and dashed lines (less reliable) show lateral correlations of similar stratigraphic heights between different sections. **(D)** Cross-section of the Khirmanjo and Shurobod sections, showing bedding directions and angles. P, Paleogene; K, Cretaceous. See (A) for the location of the cross section (I to II).

Figure 2. Stratigraphic columns of the Khirmanjo (A) and Shurabad (B) sections. See Table 1 for lithofacies codes.

Figure 3. Photos showing representative lithofacies. (**A**) Thinly bedded sandstone and mudstone interlayers, showing tabular bedding. Sandstones are massive in structure. Khirmanjo section, Shurisay Member, Baldshuan Formation. (**B**) Mudstone with interbedded thinly-bedded sandstone. Conglomerate layers outcrop as lenses. Weakly developed paleosols were observed in the mudstones. Khirmanjo section, lower Childara Member, Baldshuan Formation. (**C**) Thick conglomerate layers with interbedded mudstones. Khirmanjo section, upper Childara Member, Baldshuan Formation. (**D**) Well-developed paleosol nodules in mudstone. Khirmanjo section, Chingou Formation. (**E**) Angular, very poorly sorted, and less well-cemented conglomerate with clasts as large as >1 m. Shurobod section, Chingou Formation. (**F**) Interbedded conglomerate and mudstone, showing tabular bedding. Shurobod section, Chingou Formation. (**G**) Matrix-supported conglomerate, clasts are angular. Shurobod section, Chingou Formation. (**H**) Conglomerate bed showing erosive base. Shurobod section, Chingou Formation. KH and SB denote Khirmanjo and Shurobod sections, respectively.

Figure 4. Left panels: Orthogonal projections of progressive thermal demagnetization for selected representative samples from the Shurobod (18SB) and Khirmanjo (16KHN) sections. The red solid circles and green open circles represent projections in the horizontal and vertical planes, respectively. **Right panels**: Equal-area stereographic projection of the Characteristic Remnant Magnetization (ChRM) directions for the Shurabad section (upper panel) and Khirmanjo section

(lower panel), as in situ (left panel) and tilt corrected (right panel). Positive (negative) inclinations on the lower (upper) hemispheres are shown as solid (open) symbols. ChRM directions shown in green were iteratively rejected after a 45° cutoff from their mean virtual geomagnetic poles for reversed and normal directions, respectively. Fisher means for normal and reversed polarities (stars) are indicated with 95% ellipse.

Figure 5. Simplified lithostratigraphy and magnetostratigraphy of the Khirmanjo and Shurobod sections. The polarity of paleomagnetic directions is indicated by their reversal angle (difference between measured direction and the mean direction at the site as defined by Valet et al. (2012)). Black and white points depict paleomagnetic directions found reliable and unreliable respectively (see methods). Normal (black) and reversed (white) Polarity zones are defined by at least 2 paleomagnetic directions and intervals with only one paleomagnetic direction are shown in grey. Note that the preferred and alternative correlation imply different overlapping stratigraphic intervals between the Khirmanjo and Shurobod sections.

Figure 6. Detrital zircon U-Pb age spectra kernel density estimates (KDEs) of sandstone samples from the Khirmanjo and Shurobod sections. The grey vertical band highlights Eocene zircon ages. x0.2 in the lower two samples indicate that the highest age peak is reduced to 0.2 times of true height.

Figure 7. Temporal variations of **(A)** sediment accumulation rate, **(B)** mudstone bulk-rock εNd, **(C–D)** carbonate cement stable oxygen ($\delta^{18}O$) and carbon ($\delta^{13}C$) isotopic values. The blue points in (B) are modern river mud ε_{Nd} values from Blayney et al. (2016) and Blayney et al. (2019). Also

shown is the lithostratigraphic column. The orange solid and dashed curves in C and D are bootstrap smoothing and 1σ confidence intervals.

Figure 8. Photomicrographs under cross-polarized light (A–E). **(A)** Siltstone dominated by quartz (Q) grains and calcite cement. Shurisay Member, Baldshuan Formation. **(B)** Sandstone dominated by quartz (Q) grains, volcanic lithics, and calcite cement (shown by red arrows). Chingou Formation. **(C)** Pebbly sandstone showing a large volcanic lithic clast and surrounding fibrous calcite cement. Chingou Formation. **(D)** Sandstone dominated by quartz and sedimentary lithics (Ls), cemented by micritic carbonate. Blue arrow shows a detrital calcite grain. Chingou Formation. **(E)** Sandstone dominated by volcanic lithics and quartz, cemented by large sparry calcite. Chingou Formation. **(F)** Cathodoluminescence image of the same sample as (C) but only partial overlap (anchored by the large quartz grain). Note the homogeneous luminescence of the sparry calcite cement (red-colored). KH and SB denote Khirmanjo and Shurobod sections, respectively.

Figure 9. Comparisons of sedimentary sections in the eastern and north-eastern Tajik Basin, as well as the western Tarim Basin.

Figure 10. Compiled detrital zircon spectra (KDEs) from several different locations in the Tajik Basin. See Figure 1 for locations. Also shown are the detrital zircon U-Pb age spectra of potential source terranes, compiled from Robinson et al. (2004), Lukens et al. (2012), Carrapa et al. (2014), Blayney et al. (2016), Chapman et al. (2018), and He et al. (2018). The grey and green vertical bands show diagnostic magmatic zircon ages (Eocene vs. Cretaceous) of the Central and South Pamir, respectively. x0.2 and x0.5 indicate the highest age peaks reduced respectively to 0.2 or 0.5 times of true height.

Table 1. Summary of lithofacies observed in the Khirmanjo and Shurabad sections.

Code	Description	Interpretation
Gmm	Granule to cobble conglomerate, matrix supported, massive (disorganized), poorly sorted, subangular to rounded, 1–10 m thick, occasionally exhibiting normal grading in top part	Mass-flow deposits of cohesive debris flows
Gcm	Granule to cobble conglomerate, clast supported, massive (disorganized), moderately to poorly sorted, subangular to rounded, tabular- or lenticular-shaped, occasionally normally or inversely graded, both erosive and nonerosive base were observed	Deposits of clast-rich hyperconcentrated flows or non-cohesive debris flows
Gch	Granule to pebble conglomerate, clast supported, horizontally stratified, nonerosive base	Deposits of 'normal' shear traction flows under flood-stage conditions
Sm	Medium- to coarse-grained sandstone, massive, thinly bedded, sometimes pebbly base, tabular shaped	Sandy debris flows in channels or overbank, or heavily bioturbated sand
Sh	Medium- to coarse-grained sandstone, horizontally stratified, thin- to medium-bedded	Upper flow-regime plane bed conditions in channels, overbank, or sheet flood
St	Coarse-grained sandstone, showing trough cross-stratification	Migration of three-dimensional ripples/dunes in channels
Fm	Massive claystone to siltstone. Pebble clasts are not uncommon	Suspension deposits of waning flows in overbank or abandoned channels
Fl	Laminated claystone to siltstone	Suspension deposits of waning flows in overbank or abandoned channels
P	Massive, generally bioturbated, root traces and carbonate nodules were observed	Paleosols

Table 2. Modal petrographic and inter-granular volume (IGV) data of selected sandstone samples.

ID	Age (Ma)	Thickness (m)[#]	Detrital calcite	Carbonate cement	Matrix	Pore	Minerals & lithics	Total	IGV (%)[*]	Detrital calcite/ (detrital+cement)	Carbonate cement/total
SB254	8.2	2753	4	152	82	4	258	500	47.60	2.56%	30.40%
SB224	8.7	2576	15	134	109	11	231	500	50.80	10.07%	26.80%
SB190	9.1	2337	8	64	155	6	267	500	45.00	11.11%	12.80%
SB135	10.2	2081	4	42	120	9	325	500	34.20	8.70%	8.40%
SB80	10.8	1927	1	54	208	7	230	500	53.80	1.82%	10.80%
SB20	11.7	1498	6	129	95	6	264	500	46.00	4.44%	25.80%
SB11	12	1443	32	106	202	4	156	500	62.40	23.19%	21.20%
KHN4	11.7	1645	1	128	100	7	264	500	47.00	0.78%	25.60%

[#]Thickness in the composite stratigraphic column.

[*]IGV = (Pore + Matrix + Carbonate cement) / Total.

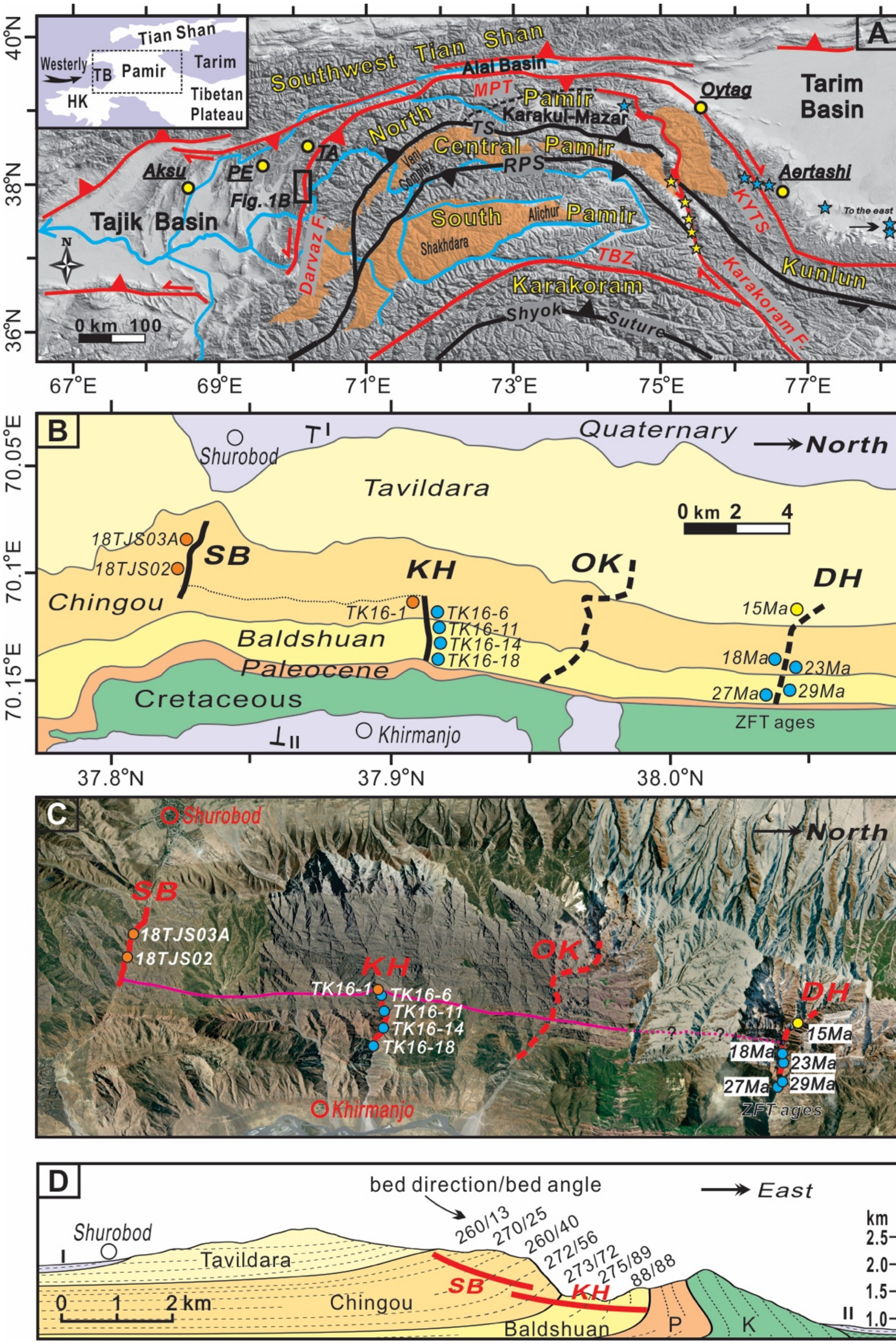
A
Tian Shan
Westerly
TB
Pamir
Tarim
HK
Tibetan Plateau
Southwest Tian Shan
Alai Basin
MPT
Pamir
Karakul-Mazar
Oytag
Tarim Basin
North
TS
Central
Pamir
RPS
Aksu
PE
TA
Fig. 1B
Tajik Basin
Darvaz F
South
Alichur
Pamir
Shakhdara
Aertashi
KYTS
To the east
TBZ
Karakoram
Kunlun
Karakoram F
Shyok
Suture
0 km 100
40°N
38°N
36°N
67°E
69°E
71°E
73°E
75°E
77°E
B
Quaternary
North
Shurobod
Tavildara
0 km 2 4
18TJS03A
18TJS02
SB
KH
OK
DH
Chingou
TK16-1
TK16-6
TK16-11
TK16-14
TK16-18
15Ma
18Ma
23Ma
27Ma
29Ma
Baldshuan
Paleocene
Cretaceous
ZFT ages
Khirmanjo
70.05°E
70.1°E
70.15°E
37.8°N
37.9°N
38.0°N
C
Shurobod
North
SB
18TJS03A
18TJS02
KH
TK16-1
TK16-6
TK16-11
TK16-14
TK16-18
OK
DH
15Ma
18Ma
23Ma
27Ma
29Ma
ZFT ages
Khirmanjo
D
bed direction/bed angle
East
Shurobod
260/13
270/25
260/40
272/56
273/72
275/89
88/88
Tavildara
SB
KH
Chingou
Baldshuan
P
K
0 1 2 km
km
2.5
2.0
1.5
1.0

Figure 1

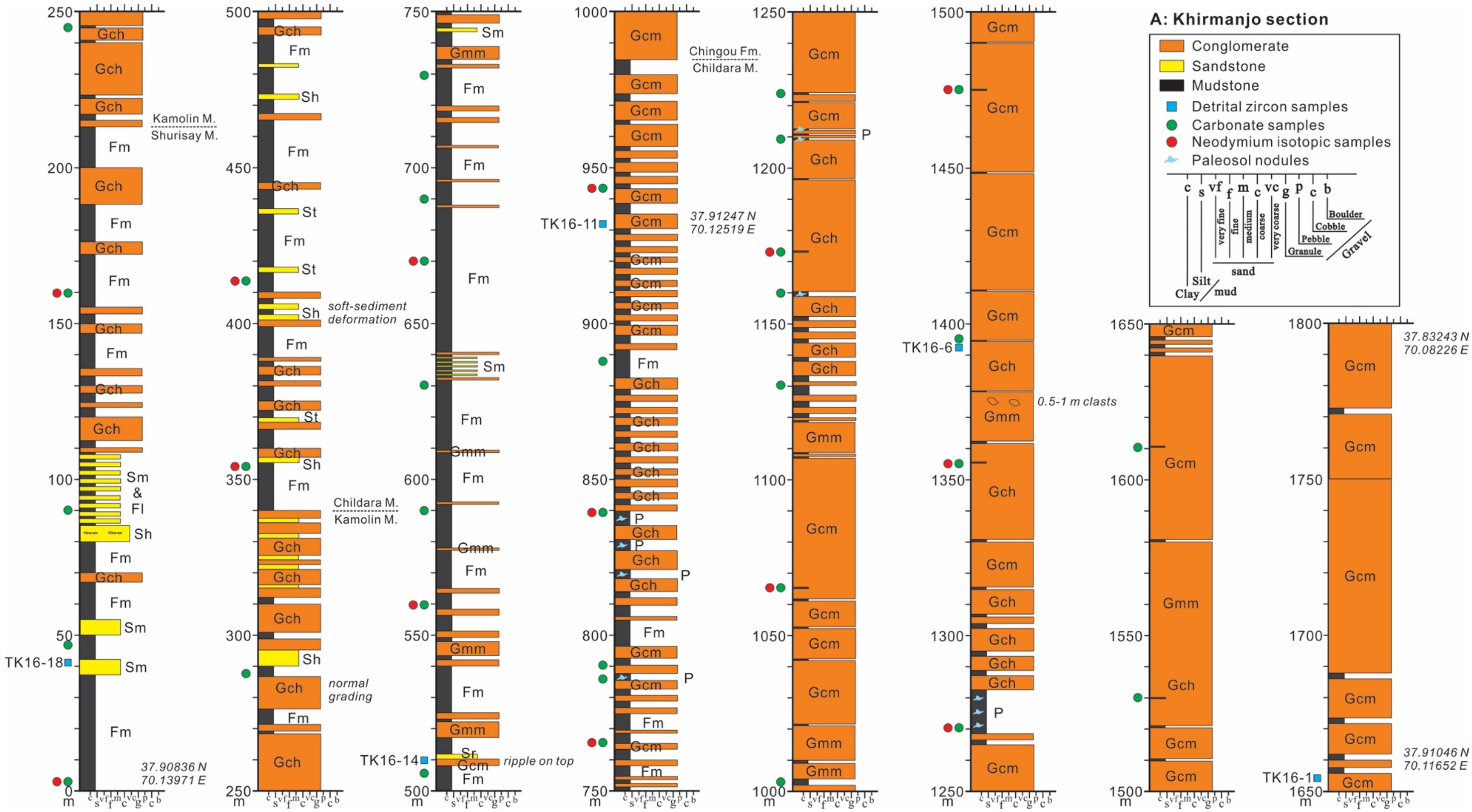
A: Khirmanjo section
Conglomerate
Sandstone
Mudstone
Detrital zircon samples
Carbonate samples
Neodymium isotopic samples
Paleosol nodules
Clay
Silt
mud
sand
very fine
fine
medium
coarse
very coarse
Granule
Pebble
Cobble
Boulder
Gravel
Kamolin M.
Shurisay M.
Childara M.
Kamolin M.
Chingou Fm.
Childara M.
soft-sediment deformation
normal grading
ripple on top
0.5-1 m clasts
TK16-18
TK16-14
TK16-11
TK16-6
TK16-1
37.90836 N
70.13971 E
37.91247 N
70.12519 E
37.83243 N
70.08226 E
37.91046 N
70.11652 E
Gcm
Gch
Gmm
Fm
Sm
Sh
St
Sr
Fl
P

Figure 2

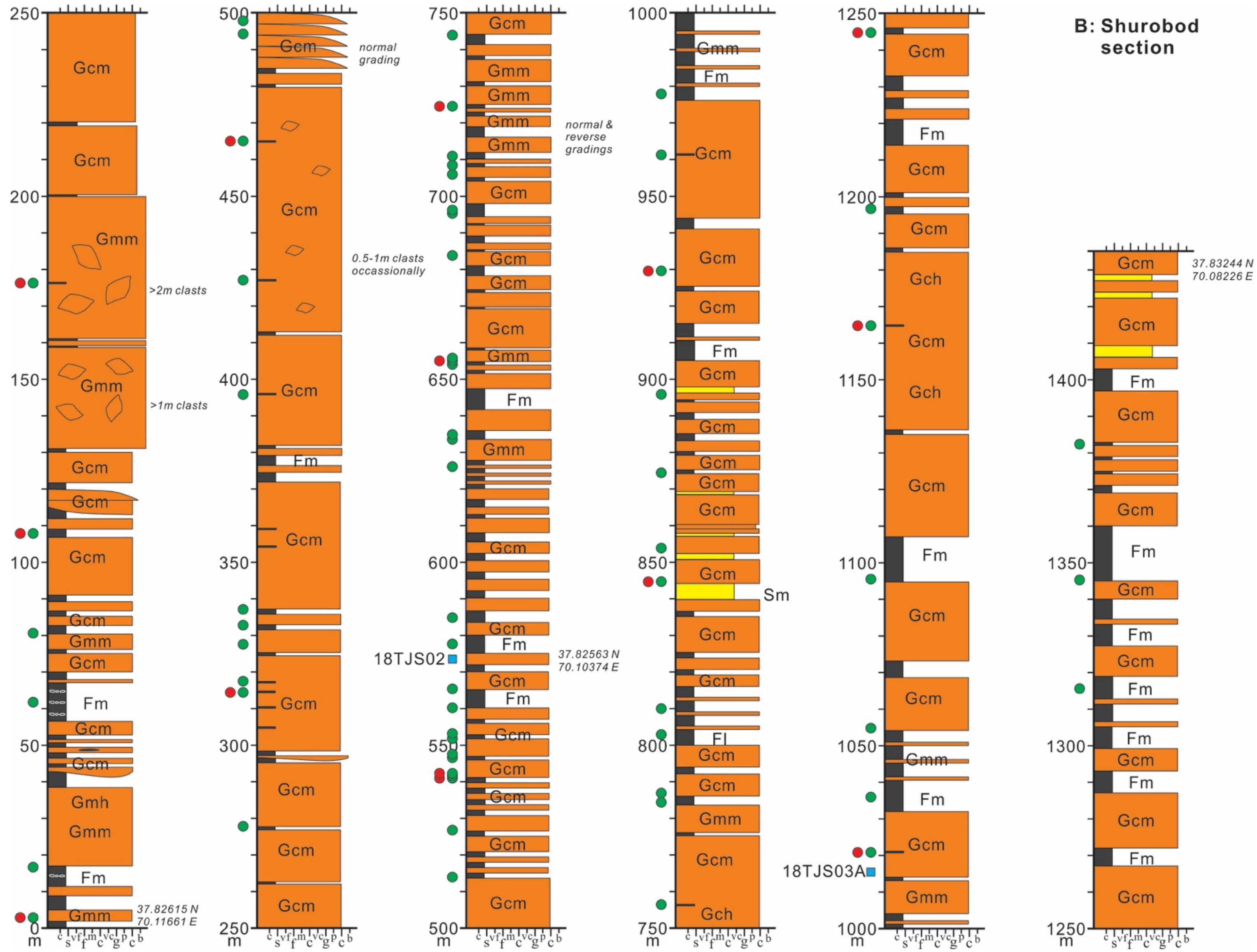

Figure 2 continued

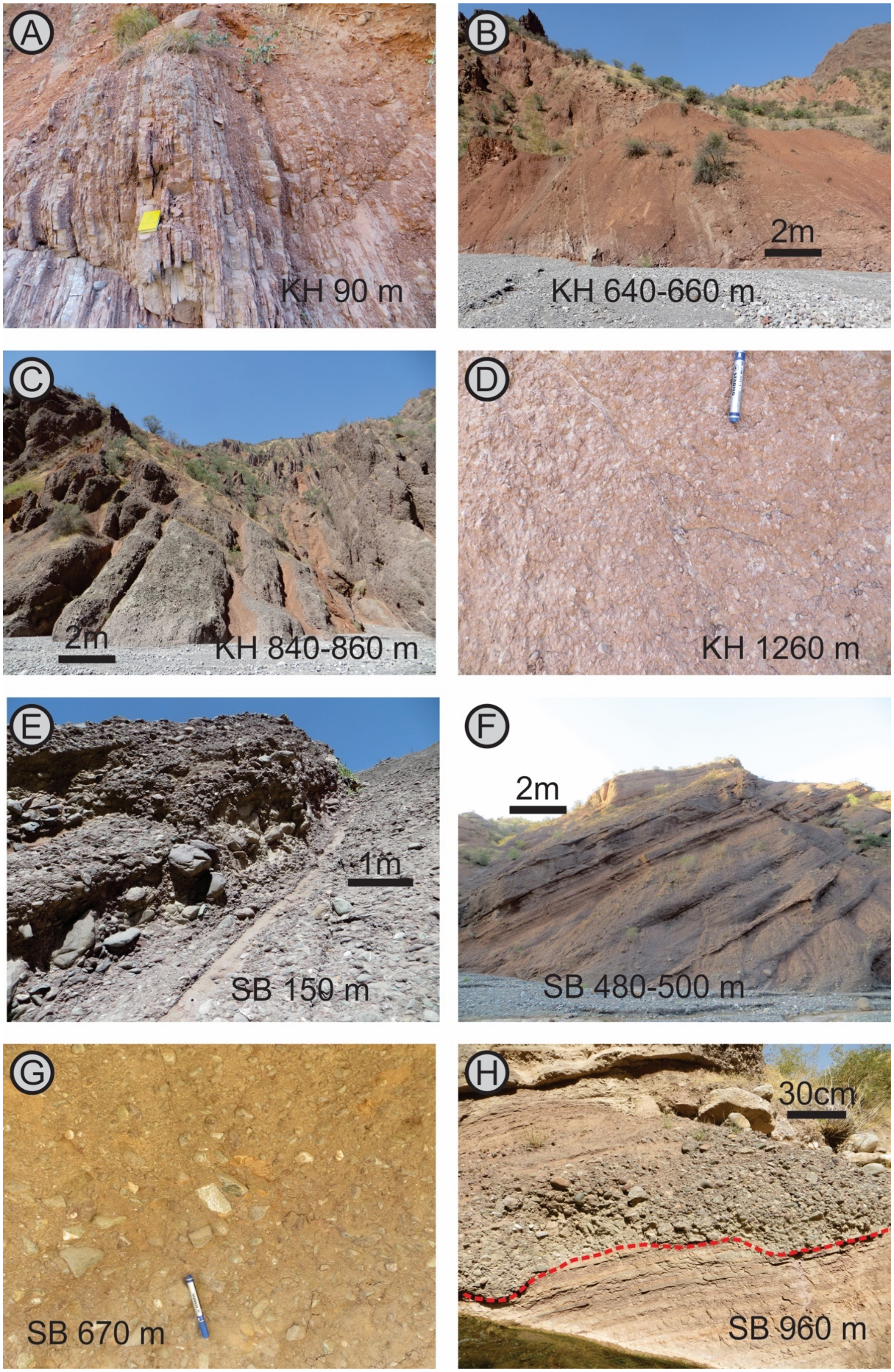
A
KH 90 m
B
2m
KH 640-660 m
C
2m
KH 840-860 m
D
KH 1260 m
E
1m
SB 150 m
F
2m
SB 480-500 m
G
SB 670 m
H
30cm
SB 960 m

Figure 3

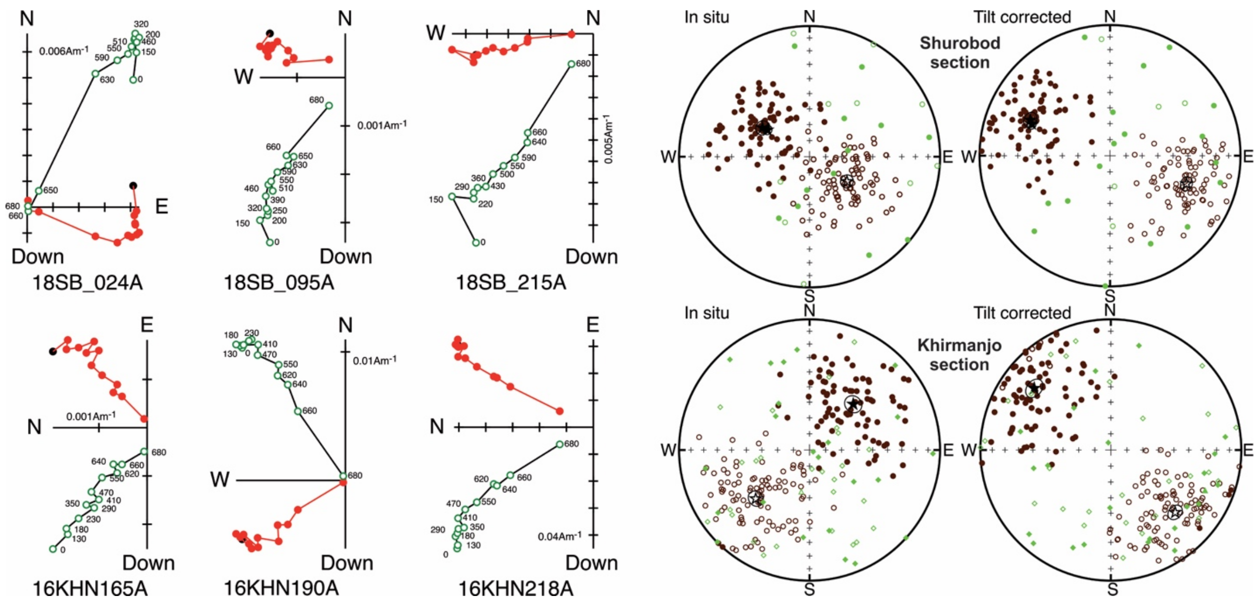
N
E
Down
0.006Am-1
18SB_095A
18SB_024A
W
0.001Am-1
18SB_215A
0.005Am-1
16KHN165A
16KHN190A
0.01Am-1
16KHN218A
0.04Am-1
In situ
Tilt corrected
Shurobod section
Khirmanjo section
S

Figure 4

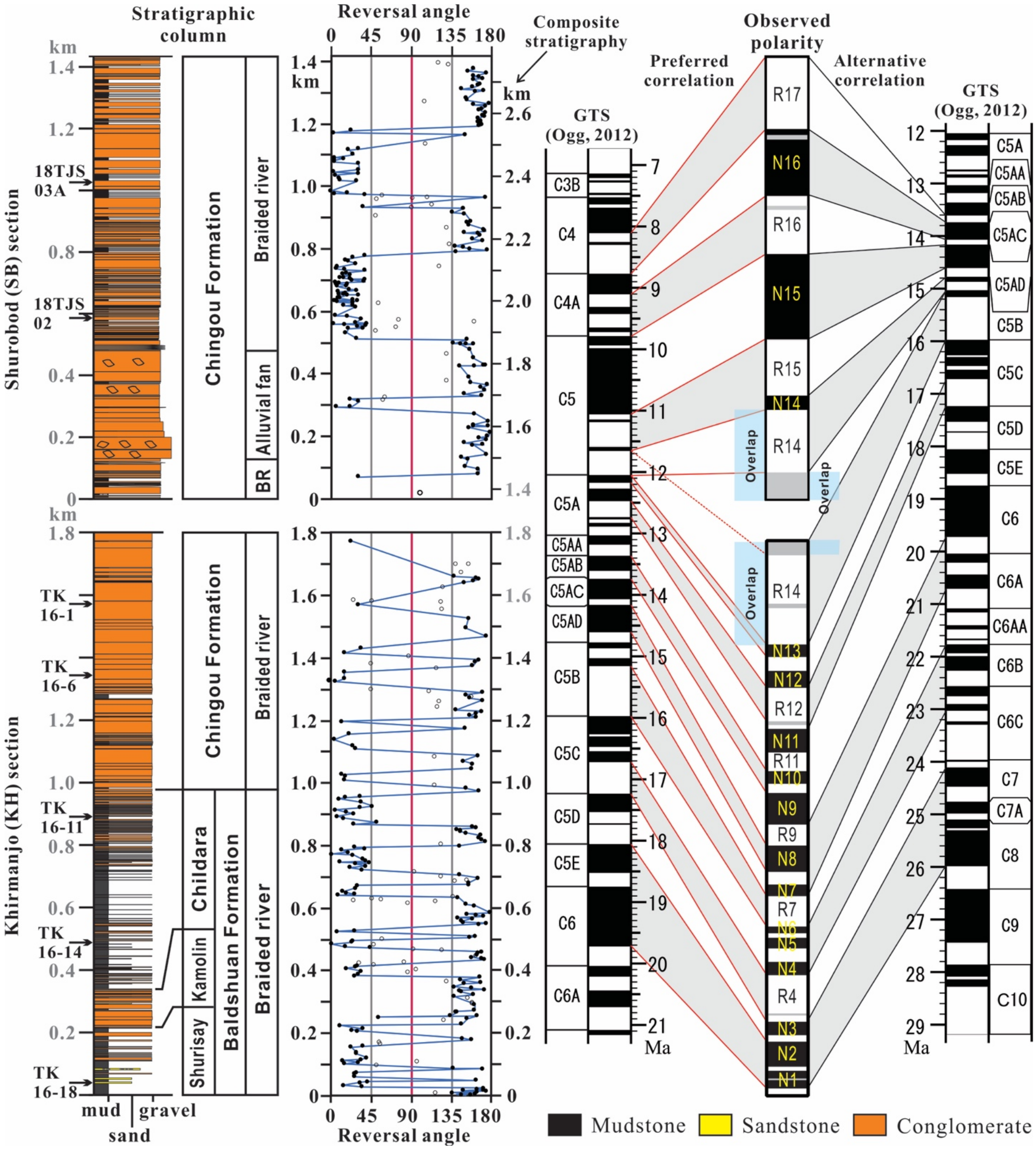
Stratigraphic column
Reversal angle
Composite stratigraphy
Observed polarity
Preferred correlation
Alternative correlation
GTS (Ogg, 2012)
Shurobod (SB) section
Khirmanjo (KH) section
Chingou Formation
Baldshuan Formation
Childara
Kamolin
Shurisay
Braided river
Alluvial fan
BR
18TJS 03A
18TJS 02
TK 16-1
TK 16-6
TK 16-11
TK 16-14
TK 16-18
mud
sand
gravel
km
Ma
Overlap
Mudstone
Sandstone
Conglomerate

Figure 5

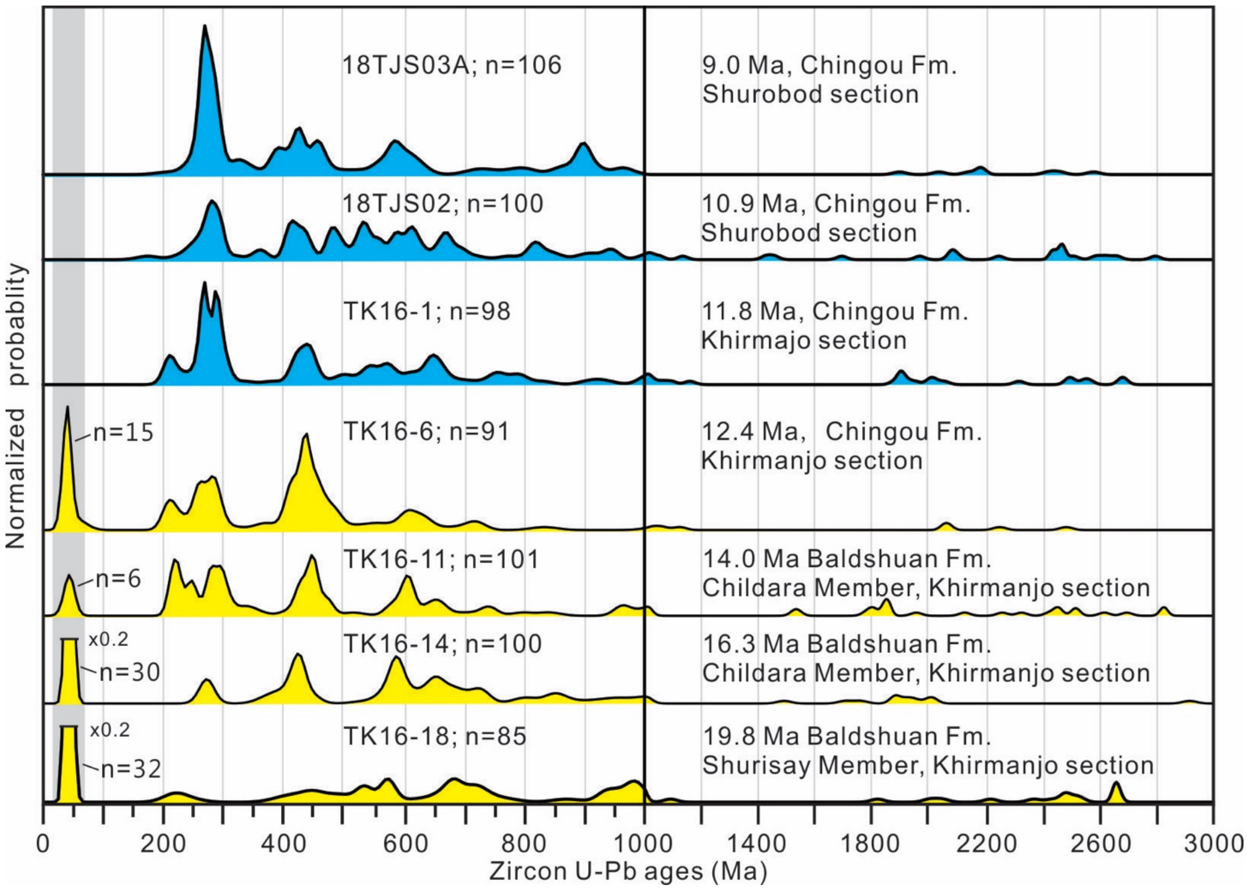
18TJS03A; n=106
9.0 Ma, Chingou Fm.
Shurobod section
18TJS02; n=100
10.9 Ma, Chingou Fm.
Shurobod section
TK16-1; n=98
11.8 Ma, Chingou Fm.
Khirmajo section
n=15
TK16-6; n=91
12.4 Ma, Chingou Fm.
Khirmanjo section
n=6
TK16-11; n=101
14.0 Ma Baldshuan Fm.
Childara Member, Khirmanjo section
x0.2
n=30
TK16-14; n=100
16.3 Ma Baldshuan Fm.
Childara Member, Khirmanjo section
x0.2
n=32
TK16-18; n=85
19.8 Ma Baldshuan Fm.
Shurisay Member, Khirmanjo section
Normalized probablity
0
200
400
600
800
1000
1400
1800
2200
2600
3000
Zircon U-Pb ages (Ma)

Figure 6

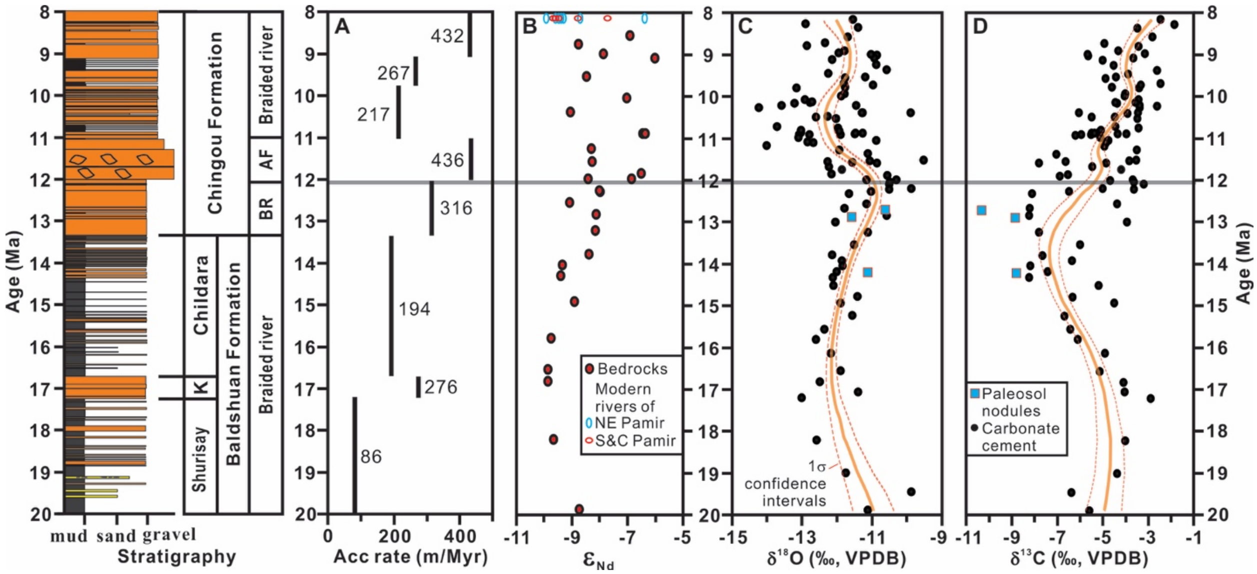
Age (Ma)
mud sand gravel
Stratigraphy
Chingou Formation
Baldshuan Formation
Childara
K
Shurisay
Braided river
AF
BR
A
Acc rate (m/Myr)
432
267
217
436
316
194
276
86
B
Bedrocks
Modern rivers of
NE Pamir
S&C Pamir
εNd
C
1σ confidence intervals
δ18O (‰, VPDB)
D
Paleosol nodules
Carbonate cement
δ13C (‰, VPDB)

Figure 7

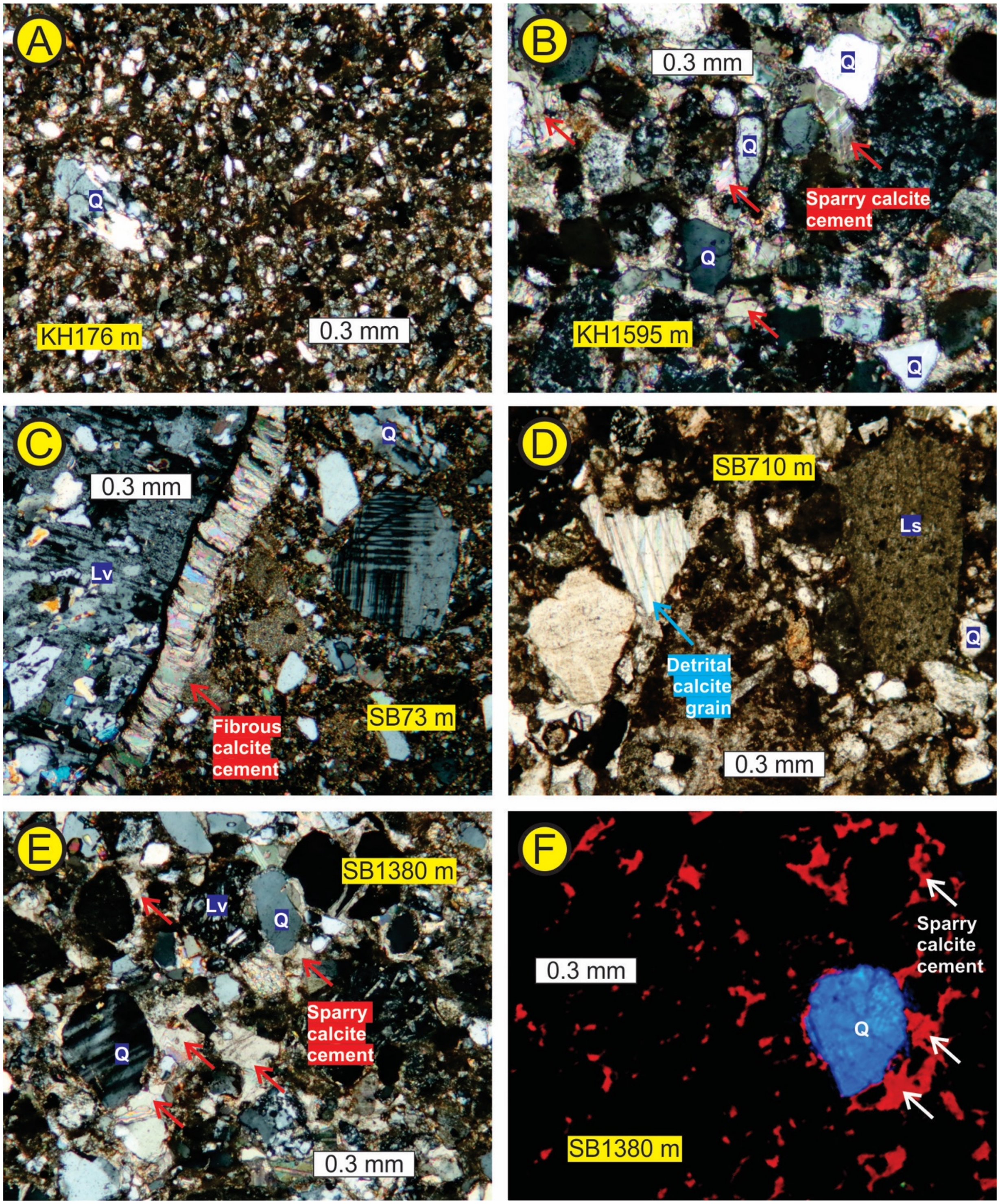

952

953 Figure 8

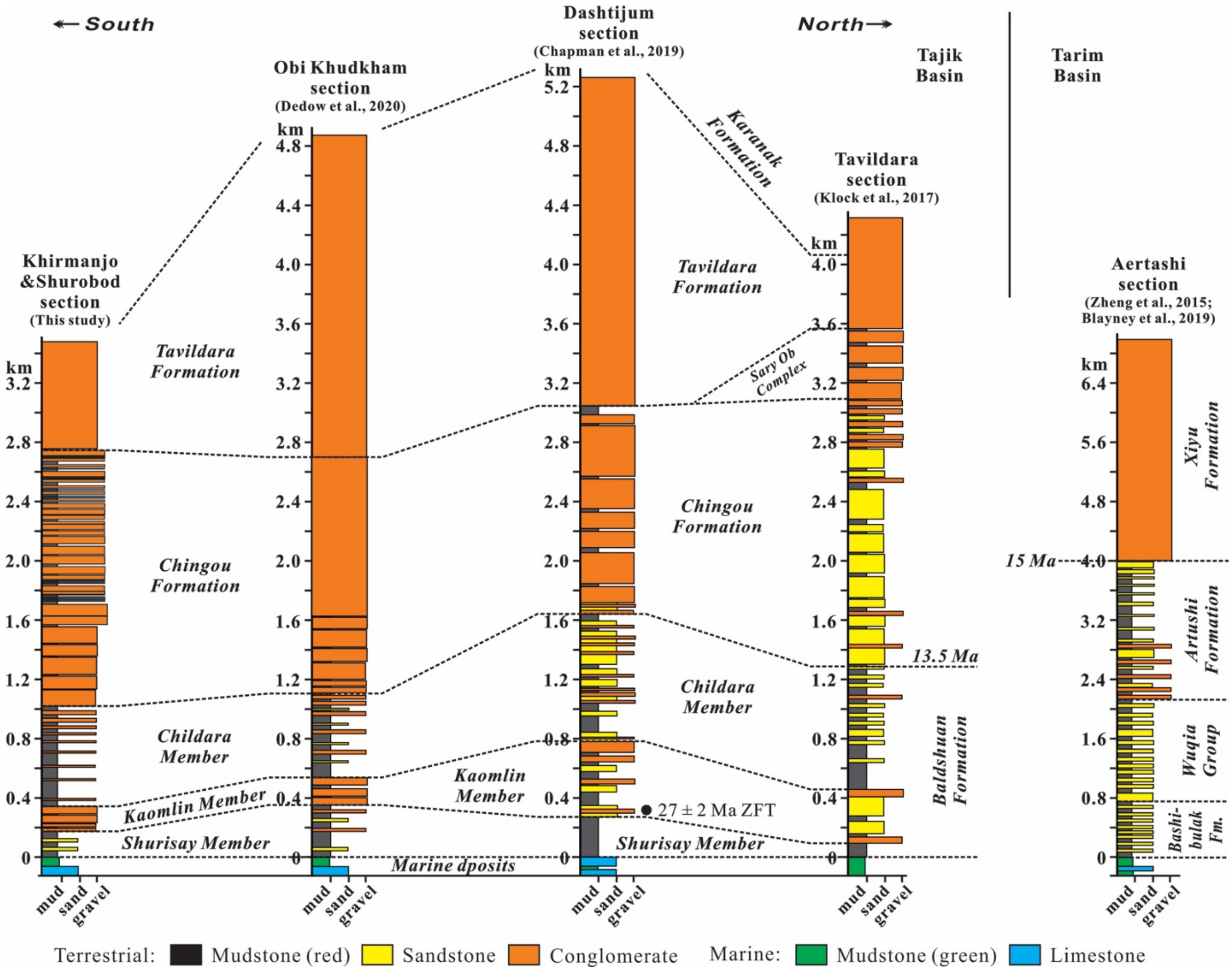
← South
North →
Tajik Basin
Tarim Basin
Khirmanjo &Shurobod section
(This study)
Obi Khudkham section
(Dedow et al., 2020)
Dashtijum section
(Chapman et al., 2019)
Tavildara section
(Klock et al., 2017)
Aertashi section
(Zheng et al., 2015; Blayney et al., 2019)
km
Karanak Formation
Tavildara Formation
Sary Ob Complex
Chingou Formation
Childara Member
Kaomlin Member
Shurisay Member
Marine dposits
Baldshuan Formation
27 ± 2 Ma ZFT
13.5 Ma
15 Ma
Xiyu Formation
Artushi Formation
Wuqia Group
Bashi-bulak Fm.
mud
sand
gravel
Terrestrial:
Mudstone (red)
Sandstone
Conglomerate
Marine:
Mudstone (green)
Limestone

Figure 9

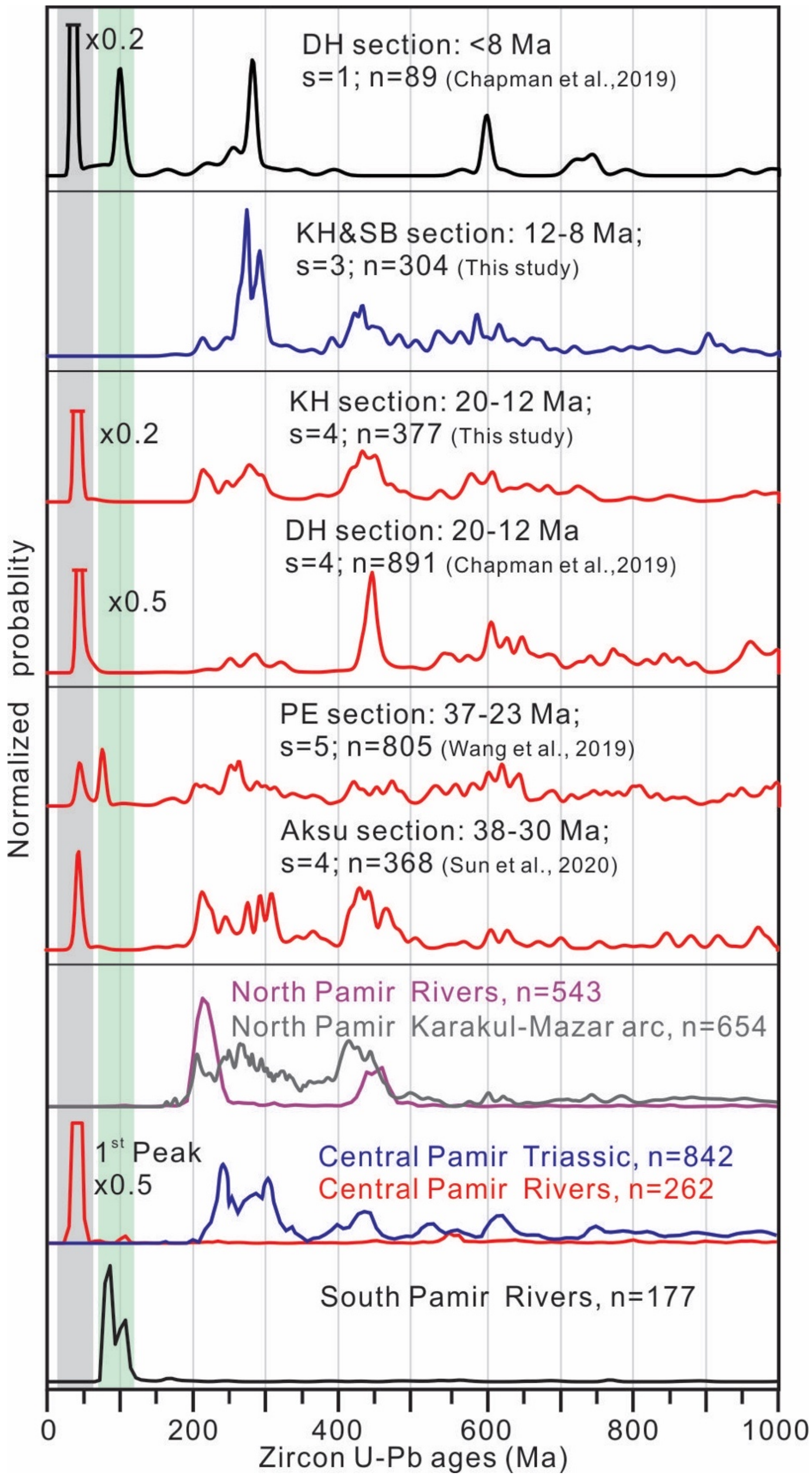
x0.2
DH section: <8 Ma
s=1; n=89 (Chapman et al.,2019)
KH&SB section: 12-8 Ma;
s=3; n=304 (This study)
KH section: 20-12 Ma;
s=4; n=377 (This study)
x0.2
DH section: 20-12 Ma
s=4; n=891 (Chapman et al.,2019)
x0.5
PE section: 37-23 Ma;
s=5; n=805 (Wang et al., 2019)
Aksu section: 38-30 Ma;
s=4; n=368 (Sun et al., 2020)
North Pamir Rivers, n=543
North Pamir Karakul-Mazar arc, n=654
1st Peak
x0.5
Central Pamir Triassic, n=842
Central Pamir Rivers, n=262
South Pamir Rivers, n=177
Normalized probablity
0
200
400
600
800
1000
Zircon U-Pb ages (Ma)

Figure 10